Altimeter observations of baroclinic oceanic inertia-gravity wave turbulence

Roman E. Glazman and Benny Cheng

Jet Propulsion Laboratory, California Institute of Technology, Pasadena CA 91109

Abstract

For a wide range of nonlinear wave processes - from capillary to planetary waves - theory predicts the existence of Kolmogorov-type spectral cascades of energy and other conserved quantities occurring via nonlinear resonant wave-wave interactions. So far, observations of wave turbulence (WT) have been limited to small-scale processes such as surface gravity and capillary-gravity waves. Presently, sea surface height measurements by the Topex/Poseidon altimeter allow one to detect WT with spatial scales from about 50 km and to a thousand kilometers - occurring in baroclinic inertia-gravity (IG) waves. The average amplitude of sea surface height oscillations is about 5 cm, which means that the internal wave amplitude is roughly 50 m. In many regions this amplitude is much greater. Similar to the case of acoustic waves generated by 3D turbulence, IG waves attain their highest intensity in regions of a large horizontal velocity shear near major ocean currents - where the level of 2D vertical turbulence is high. The degree of the IG wave nonlinearity in such regions is well above the weak-turbulence limit (of 4-wave resonant interactions): in the Gulf Stream and Aghulas Current regions, the wave spectra attain the saturation regime similar to the Phillips spectrum of surface, gravity waves on deep water. Scattering of barotropic tide by ocean floor topography provides another mechanism of baroclinic IG WT which has important implications for global dissipation of tidal energy.

Submitted to Phil. Trans. Ser. A, Roy. Soc. London. November 1996

LIST OF CONTENTS:

1. Introduction 3

2 Theoretical spectra of inertia-gravity wave turbulence 5

2.1 Direct energy cascade 6

2.2 Inverse cascade of wave action 9

2.3 Normalization of SSH spectra 10

2.4 Limitations of present theory 10

3. Effect of “noise” on altimeter-based spectra of SSH variations 11

4. Separation of motions with different time scales 12

4.1 SSH spatial variations along and between altimeter groundtracks 14

4.2. Detection of baroclinic IG WT in satellite altimeter measurements 14

4.3 Reduction of spatial noise 16

5. Analysis of baroclinic wave motions 17

5.1 Rossby waves 17

5.2 Inertia-gravity waves 20

6. The inverse problem of baroclinic IG WT 22

7. Application to the Atlantic Ocean 24

7.1 Field of baroclinic IG WT 24

7.2 Quasi-geostrophic motion 26

8. Summary and conclusions 27

ACKNOWLEDGMENTS 28

CAPTIONS FOR FIGURES 29

REFERENCES 32

FIGURES 35

1. Introduction

By wave turbulence (YVT for brevity) we understand local nonlinear resonant wave-wave interactions resulting in continuous spectral fluxes of energy and, possibly, other conserved quantities from the range of scales where the wave motion is generated by external forcing to either smaller or larger scales (e.g., Zakharov, 1984; Zakharov et al., 1992). The corresponding power spectra of fluid velocity or sea surface height (SSH) oscillations tend to be rather broad and, within selected sub-ranges of wavenumbers and frequencies, exhibit power-law behavior. In these "scale-invariant" regimes, the SSH geometry is characterized by a quasi-fractal pattern (Glazman, 1993).

A standard example of WT is the field of wind-generated surface gravity waves on deep-water: the wind energy supplied within a narrow spectral range (the "generation range") is cascaded down the spectrum due to nonlinear interactions within resonant wave tetrads (Hasselmann, 1962). Provided the wind fetch and duration are sufficiently long, an inverse cascade of wave action develops at wavenumbers below the generation range (Zakharov and Zaslavskii, 1982). Some of the energy is eventually dissipated in the high-wavenumber range due to small-scale wave breaking and viscosity and some energy is advected in the wave propagation direction due to the wave group velocity.

Many dynamical features of deep-water surface. gravity and capillary waves are expected to be found also in baroclinic IG waves because they attain a substantial degree of nonlinearity. Such features include: 1) the inverse cascade of wave action causing large-scale oscillations ("condensate") at near-inertia] frequencies (Falkovich and Medvedev, 1992), 2) the presence of several distinct power-law sub-ranges in wave spectra (Glazman, 1996), 3) intermittent events of short-length wave breaking producing small-scale turbulence, etc. The first feature is of special interest: the high kinetic energy at the inertial frequency has been observed by many authors - see (Webster, 1968) for a historic review. However, traditional explanations of this spectral peak based on linear theories (e.g., Pollard, 1970; Desaubies, 19"/3; Munk, 1980) have serious deficiencies. The IG

WT theory predicts the inertial peak as a result of the inverse spectral cascade of wave action from the shorter-scale range where the energy, action and momentum are supplied by external forcing -- similar to the case of wind-generated surface gravity waves on deep water (Falkovich, 1992; Falkovich and Medvedev, 1992; Glazman, 1996).

In contrast to the usual eddy turbulence, WT was never regarded as a key physical process for ocean dynamics. However, this perception may have to be revised. As discussed in Sect. 7, WT appears to be a universal anti well pronounced phenomenon with strong links to other components of ocean dynamics.

In the framework of shallow-water equations in the beta-plane approximation, large-scale fluid motion can be divided into two basic types: the "slow" motions - which are essentially of vertical nature - and the "fast" motions of the gravity-wave type. For numerical modeling of ocean circulation, the latter represent "computational noise, " hence they are filtered out by using the quasi-geostrophic approximation (the Charney-Obukhov-Hasegawa-Mima equation) or by imposing the rigid-lid condition at the surface (for the barotropic component). The intrinsic frequency of the fast oscillations is limited from below by the local inertial frequency $f = 2\Omega\sin\theta$, where Ω is the Earth rotation frequency and θ is the geographic latitude, whereas the characteristic timescales of Rossby waves and other quasi-geostrophic motions are measured in weeks and months, not hours. A statistical approach permitting separation of motions with different time scales is described in Sects. 4 and 5.

Although the statistical characteristics of the slow motions represent only an intermediate result of our work, they are of great intrinsic interest. Therefore, in Sects. 5 and 7 we analyze these motions and quantify intensity of the quasi-geostrophic component in the Atlantic. We also demonstrate that the Rossby wave field is characterized by a broad angular and wavenumber spectra; hence, the traditional determination of the wave phase velocity based on longitude-time plots of a low-pass filtered SSH field is fundamentally flawed and it yields a greatly overestimated phase velocity. The material in Sects. 5 and 7 facilitates our conclusion that the main source of baroclinic IG wave energy is the instability of vertical motions with respect to gravity mode perturbations.

Baroclinic IG WT has never been expected to affect satellite altimeter measurements. By design, the primary mission of satellite altimetry is to measure SSH variations associated with large-scale ocean dynamics. Hence, any substantial contribution of IG WT (except for purely periodic, tidal wave component which is routinely removed from the measured SSH signal) would encumber the primary mission of ocean altimetry and call for a re-interpretation of some of its results. The present work gives a strong ground to such concerns.

2. Theoretical spectra of IG WT

The main goal of our study is the identification of IG WT in altimeter measurements. This task is greatly facilitated given theoretical knowledge on the IG WT process. in this Section we provide a brief review of wave spectra derived in (Glazman, 1996).

Depending on the location of the external forcing in the Fourier space, nonlinear wave dynamics may be dominated either by the direct energy cascade or by the inverse cascade of wave action (Falkovich and Medvedev, 1992). If the frequency of wave excitation is greater than f but much lower than the Brunt-Väisälä frequency, the spectrum will contain both subranges. This case may be realized, for instance, at mid-latitudes where baroclinic IG waves receive (at least part of) their energy from a semi-diurnal barotropic title scattered by ocean floor topography. Using the IG wave dispersion relationship,

$$\omega = \sqrt{f^{22} + (kc)^2} \quad , \tag{1}$$

a crude estimate of the characteristic wavenumber scale for the external energy input is found as

$$k_T = R^{-1}\sqrt{(\omega_T / f)^2 - 1} - / < `J \; / \sin^2(\theta) -] \; .\cot(\theta) / R \quad , \tag{2}$$

where ω_T is the tidal frequency and R is the Rossby radius of deformation,

$$R = c / f \tag{3}$$

Here, c is the phase velocity of Kelvin waves for the 1st baroclinic mode. Using (3) in (2), we find $k_T = 2\Omega\cos(\theta)/c$. Therefore, the length of baroclinic IG waves receiving energy from tides tends to increase with an increasing latitude. In the framework of the 1.5-layer model, $c \approx \sqrt{g'H_1}$ where $g' = (\Delta\rho / \rho)g$ is the reduced gravity and H_1 is the mean depth of the thermocline. For a continuous stratification, $c = \sqrt{gh}$ where h is the "equivalent depth" for the 1st baroclinic mode. This parameter is related to the Brunt-Väisälä frequency, N, by

$$h = (NH / \pi)^2 g^{-1} \tag{4}$$

in Figs. 1-6, wavenumber k_T is marked by a box at each curve. If baroclinic IG WT is assumed to be generated by the semi-diurnal tide, the wave spectrum would be determined at $k > 2\Omega\cos(\theta)/c$ by the direct energy cascade and at $k < 2\Omega\cos(\theta)/c$ by the inverse cascade of wave action.

The theoretical spectra in this Section pertain to long internal waves of the first baroclinic mode, i.e. thermocline depth oscillations, $H_1 + h(x,t)$. The power spectrum of SSH oscillations $\eta(x,t)$ is found by multiplying the power spectrum of $h(x,t)$ by

$$\varepsilon = ((\Delta\rho/\rho)H_2/H)^2, \tag{5}$$

where Ap/p is the relative difference in the water density across the thermocline boundary, H_2 is the depth of the lower layer (in the 1.5 layer mode], $H_2/H \sim O(1)$) and H is the ocean depth. The characteristic value of ε at mid-latitudes is $E \approx 10^{-6}$.

2.1 *Direct energy cascade*

For the lowest degree of wave nonlinearity - when wave-wave interactions occur in resonant tetrads - the 2D spectrum in the direct-cascade range (omitting the angular dependence) is given by

$$F(k) = \frac{\alpha\,(H_1 R)^2\,\tilde{Q}^{1/3}}{3}\,\frac{(z-1)(z^2+7)}{(z^2-1)^{5/3} z^{5/6}}, \tag{6}$$

$$\text{where } z = 1 + (kR)^2$$

Its ID version, $F_1(k)$, is illustrated in Fig. 1. $\tilde{Q} = (R / C^3)\, Q$ is the non-dimensional spectral flux of energy, and Q is the dimensional flux of energy (per unit surface area per unit mass of water) which can be viewed as the rate of energy dissipation in the high-wavenumber range. Furthermore, α_q is the universal "Kolmogorov constant" of proportionality 'whose value is presently unknown.

As the wave nonlinearity increases, the number of resonantly interacting wave components grows, and (6) has to be replaced with a more complicated expression accounting for 5-wave and higher-order resonant interactions. Denoting the effective number of the resonantly interacting wave harmonics by v, the spectrum becomes:

$$F(k) = \frac{\alpha_q(\nu)(H_1R)^2\,\tilde{Q}^{1/(\nu-1)}}{(\nu-1)}\; 3\; \frac{(z-1)(Z^2+4\nu-9)}{(z^2-1)^{(2-3)/(\nu-1)}\, z^{5/2(\nu-1)}} \qquad (7)$$

The dependence of α_q *on v* is presently unknown. The multiwave interaction regime (i.e., v > 4) is expected to be observed in ocean regions where the IG wave intensity is sufficiently high. As will be shown in Sect.7, these are the regions of a large lateral shear in the current velocity field. Because the relative degree of the IG wave nonlinearity (with respect to wave dispersion) is highest in the high-wavenumber range of the spectrum (where the IG waves tend to become nondispersive), the multiwave interaction regime would occur first of all in the spectrum tail. An example of this regime (with v as high as 10), is illustrated in Fig. 2.

It is interesting that spectra (6) and (7) display similar trends at k > 0.1 rad/km: they approximately follow the k^{-1} power law and do not depend on the Rossby radius of deformation. This power law is confirmed by satellite altimeter observations (e.g., Le Traon et al., 1994). However, as discussed in Sects. 3 and 4, the high-wavenumber range of the altimeter-observed spectra is strongly affected by various intervening factors ("noises") which may also yield the k^{-1} behavior.

Of special interest is the case of extremely strong wave turbulence - i.e., v -> ∞. By analogy with the Phillips spectrum of surface gravity waves on deep water, the corresponding limit of (7) is called the "saturated" spectrum (Larraza et al., 1990). At sufficiently high k (such that $(kR)^2 >> 1$), equation (7) yields $F(k) \approx 4\alpha_q (H_1 R)^2 (kR)^{-6}$. The corresponding 1 D spectrum is $F_1(k)$ - k^{-5}. As shown in Sect. 7, this regime is attained in the Gulf Stream and Aghulas Current regions where high-amplitude IG waves are generated by an intense mesoscale-eddy activity.

Because of the presently poor understanding of external forcing, we cannot offer a specific formula for the energy input, although for a special case of tidal forcing such relationships have been proposed (e. g., Cox and Sandstrom, 1962; Munk, 1966; Baines, 1982).

Spectrum (6) is illustrated in Fig. 1 for several values of the Rossby radius of deformation (45, 27 and 20 km) calculated for latitudes 20, 35 and 50 degree, respectively. [Actually, we plot the 1D spectrum, $F_1(k)=\varepsilon kF(k)$, which can be compared to the 1 ID spectra of along-track altimeter measurements.] We selected the value of $\alpha_q Q^{1/3}$ in (6) that yields the correct order of magnitude for $\varepsilon kF(k)$ - as compared to the typical spectra in Fig. 12 - we used $\alpha_q^{1/3} Q$ 4.6 10^{-3} m$^{2/3}$sec^{-1}. Assuming, for instance, that the entire energy flux is due to the barotropic tide scattered by ocean floor roughness and using Munk's (1966) estimate Q - 10^{-10} m^{2}sec^{-3}, we find the Kolmogorov constant α_q - 0(10). This value is greater (by an order of magnitude) than typical Kolmogorov constants in models of turbulence (including wave turbulence). Assuming smaller values of α_q (such as α_q - 0(1)) leads to greater values of Q. Therefore, barotropic title. provides only a fraction of the IGWT energy, and most of the energy must come from Other sources.

Finally, Fig. 1 shows that, given a constant energy input Q, the wave spectrum in the "mesoscale" range is independent of the Rossby radius of deformation (hence, of the latitude). [By the "mesoscale" we tentatively call the range of wavelengths 50 to 300 km]. As follows from Fig. 1, the large-scale range of the spectrum obeys power law $k^{-0.4}$, and in the mesoscale range this spectrum rolls off approximately as $k^{-1.2}$. in most ocean regions (e.g., Le Traon et al., 1990; 1992; 1994), SSH spectra in the mesoscale range roll-off much faster than $k^{-1.2}$. Such observations agree with (7) for large v (highly nonlinear waves), Fig.2. However, as shown in Sects. 6 and 7, large values of v are rather rare in the real ocean. Finally, at wavelengths shorter than about 70 km, spectra (6) and (7) are fairly flat - approaching the k^{-1} regime - in agreement with the observations. An alternative explanation of the k-1 tail is suggested in Sect. 3.

2.2 *Inverse cascade of wave action*

The relatively fast spectral roll-off observed in the mesoscale range (e.g., Le Traon et al., 1990; 1992), $F_1(k)$ - k^{-3}, is best explained by accounting for the wave action spectral flux caused by weakly-nonlinear wave-wave interactions (Glazman, 1996). In the inverse cascade range, the 2D spectrum is

$$\};(L) = \frac{8\alpha_p (H_1 R)^2 \tilde{P}^{1/3}}{3} \frac{(z - 1)}{z^{2/3}(z^2 - 1)^{5/3}}, \tag{8}$$

where $P = P / c^2$ is the non-dimensional flux of wave action and α_p is the Kolmogorov constant of proportionality for the action flux. This spectrum (multiplied by εk to make it compatible with the measured 1D spectra) is illustrated in Fig. 3. The values of R and c for this plot are the same as those for Figs. 1 and 2, and $\alpha_p P^{1/3}$ is set to 0.21 $m^{2/3} sec^{-2/3}$ - to obtain an order-of-magnitude agreement with the observed spectra, Fig. 12. Assuming the Kolmogorov constant α_p to be of the same order of magnitude as α_q of (6), we obtain a crude estimate for the wave action flux: $P \approx 10^{-5}$ m^2/sec^2. The $k^{-10/3}$ rate of the spectral roll-off shown in Fig.3 is in good agreement with altimeter measurements.

Figures 1 and 3 demonstrate that, while being similar at low wavenumbers, spectra (8) and (6) exhibit significant differences in the mesoscale range. Except for its tail, spectrum (8) yields the best overall agreement with field observations such as Fig. 12. However, the high-wavenumber range of altimeter-observed spectra is dominated by various noises discussed in Sect. 3. Hence, it should be excluded from the comparison.

2.3 *Normalization of SSH spectra*

Because of the uncertainty in the actual values of spectral fluxes Q and P and Kolmogorov constants, comparison of theoretical spectra with field observations requires additional effort. To remove the uncertainty we shall normalize spectra as $F(k)/F(k_0)$, where k_0 -R-1: Figures 4 and 5 illustrate non-dimensional 1 D spectra

$$“(k) = \frac{kF(k)}{(1/R)F(1/R)} \tag{9}$$

for the direct and inverse cascades, respectively. A most important external parameter influencing the shape of the normalized spectra is the local baroclinic Rossby radius of deformation. As a result, spectra (9) exhibit a rather strong, monotonous dependence on the geographic latitude and no dependence on the spectral fluxes. This property will be exploited in our analysis of altimeter data.

2.4 *Limitations of present theory*

By permitting an unambiguous specification of the wavenumber scale separating the two inertial subranges, the case of tidal forcing is unique. However, the tidal forcing is not the only possible, and probably not even main, mechanism of baroclinic IG wave generation. Consequently, the relative extent of the inertial subranges and their separation scale are generally unknown. Moreover, the energy and action fluxes, Q and P, are not necessarily conservative. If, for instance, baroclinic IG waves are radiated by eddies or currents (via the instability of vertical motions with respect to gravity-mock perturbations), the external forcing would occur in a wide spectral band, resulting in a divergence of spectral fluxes in the wavenumber space,

Spectra (6) - (8) are based on a rather general, albeit heuristic, theory of wave turbulence in scale-dependent systems (Glazman, 1995, 1996). Its central assumption is the locality of resonant wave-wave interactions in the Fourier space. The theory ignores possible interactions among various baroclinic modes, and it does not account for non-local energy transfer in the high-wavenumber range of the spectrum. Indeed, in the short-wave limit the dispersion relationship (1) reduces to the acoustic-type law $\omega = kc$. In this regime, the wave nonlinearity leads to the formation of “shocks” resulting in internal wave breaking and generation of small-scale turbulence, hence in an essentially nonlocal energy transfer to smaller scales. The weakly-nonlinear version of the IG WT theory is not appropriate for this range.

In view of its many simplifications, the present theory is not expected to be in perfect quantitative agreement with field observations. We do, however, expect it to correctly describe basic trends such as the rate of spectral roll-off and the dependence of the spectrum on external factors - especially on the geographic latitude entering R.

3. Effect of “noise” on altimeter-based spectra of SSH variations

As was noticed by many investigators, the characteristic behavior of the SSH spectrum at $k \geq 0.1$ rad/km is given by $F_1(k) - k^{-1}$ (Gaspar and Wunsch 1989; Le Traon et al. 1990, 1992, 1994). As we mentioned earlier, the direct energy cascade may well be responsible for this regime. In this Section we show that error noises of altimeter measurements, such as spatial variations of the electromagnetic bias, radar propagation in the troposphere influenced by water vapor fluctuations, the instrument measuring noise, etc., offer an alternative (and rather convincing) explanation of the k^{-1} regime. This power law is known as the “shot noise” spectrum: $b(k) = Bk^{-1}$.

Let σ^2_{noise} be the component of the total SSH variance due to the noise. Since the total r.m.s. error of SSH measurements is presently believed to be about 5 cm (Fu et al., 1994), we shall use $\sigma^2_{noise} \approx 10\ cm^2$ as a crude estimate of the noise level, and employ the shot noise model for scales 10 to 100 km. The short-scale boundary of this range is near the Nyquist frequency of the Topex/Poseidon altimeter measurements, and the large-scale boundary corresponds to the scale of wind fetch variations in the open ocean which control the em. bias fluctuations. Thus, the noise-related component of the 1D spectrum is modeled as

$$b(k) = \begin{cases} Bk^{-1} & for\ k_1 > k > k_2 \\ 0 & otherwise \end{cases} \qquad (10)$$

The amplitude factor B is estimated by integrating (10) over k, which yields $B = \sigma^2_{noise} / \ln(k_2 / k_l) \approx 4cm^2$ Adding b(k) to the 1D version of the noise-free spectra (6) - (8) completes our simple model of IG WT in the presence of the small-scale noise.

Of particular interest is the case when the spectrum is dominated by the inverse cascade. This is illustrated in Fig. 6. Also shown are three power laws approximating the spectrum in different sub-ranges. Comparison of this, noise-affected, spectrum with the noise-free spectrum in Fig.2 indicates that at wavenumbers above 0.01 rad/km, the inverse cascade spectrum is easy to confuse with spectrum (7). One important difference is the degree to which the Rossby radius influences these spectra: variations of R have a greater effect on the inverse cascade spectrum than on the direct cascade spectrum. In Section 6 we demonstrate that the inverse cascade spectrum with noise, Fig. 6, describes the observed R-dependence more faithfully than do spectra (6) and (7).

In summary, the characteristic features of IG WT to be detected in SSH spectra at mid-latitudes include: a very slow spectral fall-off (at the rate near $k^{-0.4}$) at wavenumbers below -0.01 rad/km; an accelerated spectral fall-off (at the rate near k^{-3}) in the range -0.02.-0.08 rad/km; a relatively slow spectral fall-off (at the rate near k^{-1}) at wavenumbers above -0.1 rad/km. This "three-segment" shape was pointed out by LeTraon et al. (1994) as typical of altimeter-reported spectra at mid latitudes. As one of most prominent features of IG WT spectra we also indicate their strong dependence on the baroclinic Rossby radius of deformation - expressed as the "blue" shift of the entire shape with the geographic latitude increasing poleward.

4. Separation of motions with different time scales

Generally, observation of IG waves is a formidable task, for it calls for accurate, simultaneous, high-spatial-density, measurements over large ocean areas - many hundreds kilometers in extent. The amplitude of SSH oscillations due to long internal waves is only about 10^{-3} times that of the thermocline depth oscillations, hence is under 10 cm, whereas the accuracy of SSH measurements by the T/P altimeter is about 5 cm in terms of the r.m.s. error. An intense background of diverse dynamical processes further complicates the problem. In order to extract information on baroclinic IG waves, one has to start with filtering out all Rossby wave modes and other types of geostrophic and quasi-geostrophic ("slow") motions. As discussed in this Section, this can be achieved by combining 1D spectra of SSH variations along altimeter groundtracks with 2D spectra of SSH variations between tracks. The procedure exploits the large intrinsic difference in the temporal autocorrelation radii of quasi-geostrophic versus gravity-mode oscillations.

The spatio-temporal autocorrelation function of altimeter-observed SSH field, on the assumption that SSH variations caused by slow and fast motions are uncorrelated, can be presented as a sum of two components

$$W(r,\tau) = W_{slow}(r,\tau) + W_{fast}(r,\tau) \tag{11}$$

For $\tau > \tau^*$, where τ^* is the characteristic autocorrelation timescale of the fast processes, $W(r,\tau) \approx W_{slow}(r,T)$. This allows one to separate motions with different timescales. Furthermore, baroclinic IG waves are not the only contributor to $W_{fast}(r,\tau)$. Being interested in $W_{IG}(r,$ ‘c), we shall treat other fast components as "noise" and assume them to be uncorrelated with IG wave oscillations: $W_{fast}(r,\tau)$ “ $W_{IG}(r,\tau) + W_{noise}(r,\tau)$.

For a few exceptions discussed in Sects. 6 and 7, $W_{noise}(r,\tau)$ should be appreciable, only at sufficiently short temporal and spatial lags. In particular, the contribution to $W_{noise}(r,\tau)$ of barotropic gravity waves is negligible for time lags τ exceeding the temporal autocorrelation radius of this wave process (while r may be as small as wc please). This timescale is practically a few wave-periods long, hence is about an hour. Similarly, when the spatial lag exceeds the autocorrelation length of altimeter measuring errors, contribution of measuring error noises becomes negligible compared to $WIG\ (r,\tau)$ at any time lag.

These properties are exploited in our data analysis procedure.

4.1 *SSH spatial variations along and between altimeter groundtracks*

SSH is sampled by the T/P altimeter every 6.4 km along a groundtrack, and a 1000 km segment of a groundtrack is covered in less than 3 minutes. Due to this, virtually instant sampling feature, IG WT (representing the fast component of SSH variability) is detectable in the 1D spectra and autocorrelation functions estimated based on individual satellite passes. However, these functions also contain information on slow motions.

The situation with 2D autocorrelation functions and spectra is different. To estimate these functions, one must simultaneously use SSH measurements from several (ascending as well as descending) passes within the ocean area of interest (such as, for example, a 10 by 10 degree square area) - as suggested in (Glazman et al., 1996a; thereafter abbreviated as GFG'96). The ascending (or descending) T/P altimeter groundtracks are about 300 km apart, and the orbit-repeat cycle is about 10 days. Time differences between SSH measurements sampled on different satellite passes within a single orbit-repeat cycle range from several hours to 10 days. Therefore, we can select pairs of SSH measurements with time differences greater than the temporal autocorrelation radius τ^* of IG wave oscillations. It is easy to show that $\tau^* \approx (2\pi/\omega_0)n$ where $\omega_0 > f$ and $2 < n < 10$, hence τ^* is small by comparison to the timescale of quasi-geostrophic motions. The 2D autocorrelation functions (and the resulting spectra) based on such measurements are affected only by the slow motions. Combined with the. 1 D "along-track" spectra, these 2D spectra allow one to extract information on the fast SSH component.

The joint analysis of along-track and between-track spectra is possible only if the resolution of the. 2D analysis is comparable to that of the 1D analysis. This is an extremely difficult requirement. The 2D spectral analysis technique developed in GFG'96 allows one to resolve spatial scales as short as 70 km.

4.2 *Detection of baroclinic IG* **WT** *in satellite altimeter measurements*

The data analysis procedure includes the following steps:

Step 1. Estimate the 1 D ("along-track") spatial autocorrelation function,

$$W(r) = <\eta(s+r)\eta(s)>, \qquad (12)$$

using altimeter measurements on individual satellite passes within a given ocean area. Because both $\eta(s)$ and $\eta(s+r)$ belong to the same satellite pass, their time difference is ignored. By the spatial lag r we understand here the distance between two points on a groundtrack, and s is the distance alongtrack from some point of reference. The products are binned by values of r. Although the data from ascending and descending passes are used separately, function W(r) is eventually obtained by averaging products $\eta(s+r)\eta(s)$ from all passes within the area under consideration. Because ascending and descending passes have different orientation, the averaging suppresses effects of the SSH fields' an isotropy. The averaged products represent an estimate of the 1 D autocorrelation function for a linear section of an equivalent isotropic spatially-homogeneous random field.

The corresponding 1D spectra were estimated as FFT of W(r) as well as directly from the SSH data in the usual manner (e.g., LeTraon et al., 1990). Both approaches yielded virtually the same results. The directly obtained spectra were then improved in the high-wavenumber range by correcting for the effect of discrete sampling (every 6.4 km) of the SSH field on individual satellite passes. To this purpose, we divided the spectrum estimate by $(\sin(kL)/kL)^2$ where $L = 6$ km.

Step 2. Estimate the 2D spatial autocorrelation function, $W_{slow}(\mathbf{r})$, based on SSH measurements taken at least two (but no more than 10) days apart. Using data from different pairs of satellite passes, wc calculate the mean of all products $\eta(\mathbf{x}+\mathbf{r},t+\Delta t)\eta(\mathbf{x},t)$ for pre-set bins on the r-plane. Actual time differences Δt between SSH measurements depend on the satellite orbit configuration and on our choice of satellite passes. Since $\eta(\mathbf{x}+\mathbf{r},t+\Delta t)$ and $\eta(\mathbf{x},t)$ belong to different passes, time lags Δt are typically much greater than the period of IG waves. Consequently, $\Delta t \geq \tau^*$ and the influence of IG waves on $W_{slow}(\mathbf{r})$ is negligible. Limiting Δt by five (or even 10) days, we ultimately ignore time differences Δt and average all SSH products as if $\eta(\mathbf{x}+\mathbf{r},t+\Delta t)$ and $\eta(\mathbf{x},t)$ were measured simultaneously. Apparently, the resulting $W_{slow}(\mathbf{r})$ is suitable for analysis of quasi-geostrophic motions because their characteristic timescale is always much larger than our At.

Step 3. Reduce $W_{slow}(\mathbf{r})$ to the 1 D form compatible with W(r), by averaging $W_{slow}(\mathbf{r})$ over the azimuthal angle:

$$W_{slow}(r) = (1/2\pi)\int_{-\pi}^{\pi} W_{slow}(r,\theta)d\theta \tag{13}$$

It is easy to show that, for a statistically isotropic SSH field, the resulting 1D function has the same meaning as the autocorrelation, W(r), of SSH oscillations along a straight line. However, a realistic SSH field is not statistically isotropic. Hence, the compatibility of (12) and (13) may not be as high as desired. Finally, the difference between (12) and(13) represents the spatial autocorrelation function of the fast motions:

$$W_{fast}(r) = W(r) - W_{slow}(r) \tag{14}$$

Except for Step 3, details of our approach (including error analysis) are given in GFG'96.

The wavenumber spectra F(k) and $F_{slow}(k)$ corresponding to W(r) and $W_{slow}(r)$ are obtained as FFT of the autocorrelation functions. In doing so, we use the Hanning window to alleviate adverse effect of the finite range of r. Finally, the inverse Fourier transform of the spectrum of the difference, $F_{fast}(k) = F(k) - F_{slow}(k)$, was compared to $W_{fast}(r)$ of (14) to ensure the correctness of the numerical scheme. Examples of functions W(r), $W_{slow}(r)$, $W_{fast}(r)$ and their Fourier transforms are illustrated in Figs. 9 and 10.

4.5' *Reduction of spatial noise*

Small-scale surface roughness fluctuations cause rapid oscillations of the measured SSH because they result in short-scale variations of the altimeter sea state bias (e.g., Branger et al., 1993). This and other factors of spatial noise are responsible for a sharp peak in the autocorrelation function W(r) in the vicinity of r=0. However, this noise-related peak can be removed by extrapolating the behavior of W(r) from larger scales - dominated by the "signal of interest" - into the small-scale range dominated by noise.. In doing so, one must respect a fundamental property of the autocorrelation function of a spatially-homogeneous random field - the requirement that W(r) behave as

$$W(r)|_{r\to 0} \approx W_0 - Cr^2 \quad , \tag{15}$$

where W_0 and C are constants. Thus, the autocorrelation function at short scales is replaced by parabola (15) whose coefficients are determined empirically using values of W(r) at sufficiently larger.

To determine W_0 and C for the along-track autocorrelation function, we used W(r) from the range $20< r \leq 40$ km. The same task for the autocorrelation function of slow motions, $W_{slow}(r)$, requires r in the range 60 to 100 km because the spatial sampling of "between-track" SSH values is much coarser than that of the along-track sampling. In either case, constants W_0 and C are determined by a least-square fit.

5. Analysis of **baroclinic wave** motions

In this Section wc present a few sample calculations to illustrate the approach. The focus is on the physical meaning and correct interpretation of the statistical quantities involved.

5.1 *Rossby waves*

Although our main task requires only the spatial autocorrelation $W_{slow}(\mathbf{r})$, we undertook a small additional effort and estimated a more general, spatio-temporal autocorrelation function $W_{slow}(\mathbf{r},\tau)$, using the technique described in GFG'96. Apparently, $W_{slow}(\mathbf{r}) = W_{slow}(\mathbf{r},0)$. Function $W_{slow}(\mathbf{r},\tau)$ facilitates our present analysis of Rossby waves and affords and insight into the physical causes of SS11 variations reflected in $W_{slow}(\mathbf{r})$.

A few examples of $W_{slow}(\mathbf{r})$ and $W_{slow}(\mathbf{r},\tau)$ are given in GFG'96 along with analysis of statistical errors in our estimates. Presently, we illustrate three sections of $W_{slow}(\mathbf{r},\tau)$ for a 10 by 10 degree surface patch centered at 300S and 5^0E (over the Walvis Ridge), Fig. 7, and for another patch at 30°S and 25°W, Fig. 8. The following review facilitates correct interpretation and utilization of these plots.

The 3D autocorrelation function of a wave field is related to its 21) wavenumber spectrum, F(k), by

$$W(\mathbf{r},\tau) = \int F(\mathbf{k}) e^{i\mathbf{k}(\mathbf{r}-\mathbf{c}(\mathbf{k})\tau)} d\mathbf{k} \qquad (= W(\mathbf{r}-\mathbf{c}\tau)), \qquad (16)$$

where c(k) is the wave phase velocity. The last equality is valid either for non-dispersive (i.e., $\mathbf{c}(\mathbf{k})$=const) or purely monochromatic (i.e., F(k) - $\delta(\mathbf{k}-\mathbf{k}_0)$) waves. The right-hand side of (16) means that the main maximum of the 3D autocorrelation function appears as a "jet" (with fuzzy boundaries) passing through the origin, Its orientation in the $\mathbf{r}$-τ space yields the vector of the wave phase velocity: c = r(z)/ τ where $\mathbf{r}(\tau)$ is the position of the autocorrelation maximum at time τ. As $(\mathbf{r}-\mathbf{c}\tau)$ increases, $W(\mathbf{r}-\mathbf{c}\tau)$ reaches its local minima and then attains secondary maxima. As shown in Figs. 7 and 8, plane sections of $W(\mathbf{r}-\mathbf{c}\tau)$ resemble a washboard.

By definition, the phase velocity vector is $\mathbf{c}=\omega/\mathbf{k}$. This is identical to $\mathbf{c} = \omega\mathbf{k}/k^2$ where k is the magnitude of the wavenumber vector. Dividing the numerator and denominator of x- and y-components of c by k_x^2 and k_y^2, respectively, the orthogonal components can be presented in the form

$$c_x = \frac{\omega/k_x}{1+\tan^2\phi} \equiv \frac{\omega}{k}\cos\phi, \qquad c_y = \frac{\omega/k_y}{1+\cot^2\phi} \equiv \frac{\omega}{k}\sin\phi, \qquad (1\text{-}7)$$

where $\tan\phi = k_y/k_x$. If the meridional component of the velocity vector is small compared to the zonal component, i.e., $\phi \to 0$, the first equation of (17) reduces to $c_x \approx \omega/k_x$. Let us show that the meridional (r_y=0) section of the autocorrelation function yields ω/k_x. As follows from (16),

$$W(r_x,0,\tau) = \int F_1(k_x) e^{i(k_x r_x - \omega\tau)} dk_x = W(r_x - (\omega/k_x)\tau), \qquad (18)$$

where $F_1(k_x) = \int F(\mathbf{k}) dk_y$ is the 1D spectrum, and the last equality is valid under the same condition as the rightmost part of (16). According to (18), the tilt r_x/τ of the main ridge of $W(r_x,0,\tau)$ (observed in the top panel of Figs.7 and 8) equals ω/k_x. - Therefore., under the condition $(k_y/k_x)^2 \ll 1$, function $W(r_x,0,\tau)$ yields an estimate of the zonal component, c_x, of the wave speed. If, however, the meridional component of the velocity vector is appreciable, the difference between ω/k_x and c_x may become quite large. For instance, for waves propagating at ±45^0 away from the zonal direction, "speed" r_x/τ

estimated based on $W(r_x, 0, \tau)$ is twice the actual c_x. The azimuthal angle ϕ for the case illustrated in Fig. 7 is about 55^0. Therefore, the meridional component of the wave vector exceeds its zonal component. This has a simple explanation as a result of Rossby wave poleward refraction caused by a rapid decrease of the Rossby radius of deformation away from the equator. Many patches *in* the Atlantic show patterns similar to those in Figs.7 and 8. Therefore, using only the meridional section, r_y=0, of the autocorrelation function - upper panel of Figs.7 and 8- would result in a substantial, systematic overestimation of the Rossby wave speed - by a factor of 2 or greater.

The same overestimation of the zonal component takes place when one uses a more conventional technique of Rossby wave analysis - the longitude-time plots of SSH variation (e.g., Chelton and Schlax, 1996). Indeed, the characteristic tilt x/t of the elongated features seen in those plots yields ω/k_x because those features are treated by Chelton and Schlax (1996), as well as by many other authors, as phase isolines (i.e., "wave crests" and "troughs") of monochromatic long waves propagating strictly westward. Another common error of this analysis is the interpretation of the distance, L_x, between neighboring "wave crests" on the x axis as the wavelength of Rossby waves. The actual wavelength, λ, is related to this distance by $\lambda = L_x \cos \phi$, hence is only about one half (or even less) of the reported value.

In general, oceanic Rossby waves are neither monochromatic nor do they propagate westward. The broad-band nature of the wave spectrum is especially well pronounced in the bottom panels of Figs.7 and 8. The short-scale region of W(r), confined by an ellipse centered at the origin and whose major axis is near horizontal with the half-length about 200 km, corresponds to a system of relatively short-scale variations. These include short Rossby waves. The larger-scale portions of W(r) - visible in Fig. 7 as chains of tilted elongated "hot" blobs indicate the presence of long Rossby waves moving, on the average, in the south-west direction. This is confirmed by the middle panel - $W(0, r_y, \tau)$ - of Fig.7. The W(r) and $W(0, r_y, \tau)$ of Fig. 8 do not show such a clear meridional component of the long Rossby wave speed. Rather, these pictures display interference patterns caused by several wave systems propagating in different directions. We thus conclude that the Rossby wave field contains waves of many different scales propagating in different directions. The strong refraction of Rossby waves caused by the latitudinal variation of the Rossby radius of deformation makes it impossible for waves generated at the eastern boundary of an ocean to cross the entire ocean basin and reach its western boundary. Therefore, the corresponding concept of the "transit time" (e.g., Chelton and Schlax, 1996) appears to be devoid of geophysical significance.

Rossby waves can be viewed approximately as non-dispersive only if $kR << 1$. At the latitude of Figs.7 and 8 (i.e. at 30^0S), the 1st baroclinic Rossby radius of deformation is about 40 km (e.g., Houry et al., 1987). Therefore, the last equality in (16) is relevant only for wavelengths substantially greater than 1000 km. Our Figs.7 and 8 do not rule out the existence of such long wave.s, although they do not show them. What these plots show very clearly is that the most energetic components of the Rossby wave spectrum belong to the wavelength range 200 to 500 km -- too short to interpret c in (16) as the phase velocity vector. The correct interpretation of the "mean wave propagation velocity" derived based on the tilt of the ridges in Figs. 7 and 8 requires numerical analysis of the integral in (16) - hence, a detailed knowledge of the wavenumber spectrum F(k) of quasi-geostrophic motions. This task is far beyond the scope of the present work.

S.2 *Inertia-gravity waves*

As explained earlier, estimation of IGWT spectra involves the use of 1D autocorrelation function $W_{slow}(r)$ obtained from $W_{slow}(\mathbf{r})$ by angular integration (1 3). To eliminate the influence of short-scale noises, we replace $W_{slow}(r)$ in the vicinity of the origin by parabola (15) and interpret W_0 as the component of the total SSH variance associated with quasi-geostrophic (including Rossby waves) motions. Examples of this "filtered" autocorrelation function are shown as dotted curves in Pane] A of Figs. 9 and 10.

The 1D autocorrelation function, $W(r)$, of SSH oscillations along altimeter groundtracks is illustrated by the solid curve in Panel A of Figs. 9 and 10. Comparison of the Fourier transform of these functions, Panel B, with the 1D wavenumber spectra estimated by Le Traon (1992) based on Geosat altimeter observations (and by Le Traon et al. (1994) based on Topex/Poseidon measurements) shows very good agreement. The difference between $W(r)$ and $W_{slow}(r)$ is shown by the dashed curve in Panel A of Figs. 9 and 10.

Panel B of Figs. 9 and 10 presents 1D wavenumber spectra related to the curves in Panel A. The SSH variance component due to the fast part of the SSH field is estimated as coefficient W_0 in (15) for $W_{fast}(r)$. In Sects. 6 and 7 we show that in most cases the spectra of the fast motions agree with the IG WT theory predictions. Therefore, we interpret $W_0^{1/2}$ as the characteristic amplitude of baroclinic IG waves and denote it by σ_{IG} in the subsequent discussion. Although the short-scale asymptotic of $W_{fast}(r)$ is not presented in Figs. 9 and 10, an estimate of W_0 (shown by the black circle on the vertical axis) can be inferred by visual examination of the dashed curves in Panel A: we find W_0 by extending the larger-scale behavior of the dashed curves to the small-scale region. The distribution of σ_{IG} for the Atlantic is presented in Fig. 11, and Fig. 12 illustrates spectra of the fast SSH component. These Figures are discussed in detail in Sect. 7.

The reader may notice that the (low-pass filtered) autocorrelation functions, $W_{slow}(r)$, and spectra of quasi-geostrophic motions for the two ocean regions in Figs. 9 and 10 are rather similar. However, in the case of the fast component (dashed curves) these characteristics are quite different: the characteristic amplitude of the fast motions in the eastern part of the Atlantic is much greater than that in the central part where it is comparable to the amplitude of quasi-geostrophic motions, σ_R.

6. The inverse problem of baroclinic IG WT

In order to justify our interpretation of $F_{fast}(k)$ as the IG WT spectra, we must show that these spectra agree with the predictions of Sect. 2. As discussed earlier, the IG WT spectrum depends on the local Rossby radius of deformation and other external factors. Owing to these-dependencies, $F_{fast}(k)$ must exhibit geographic and seasonal variations. Focusing our attention on the dependence of the spectrum on the Rossby radius of deformation, we shall now examine geographic variations of the observed spectra and compare them with theoretical trends.

Typical values of R for the North and South Atlantic are plotted in Fig. 13 based on the analysis of water density profiles by Emery et al. (1984) and Houry et al. (1887). As follows from (3) and (4), the range of possible values of R is determined by the Brunt-Väisälä frequency and ocean depth: NH should remain within reasonable limits - such that the equivalent depth is constrained by $0.5 < h < 1.0$ m. The corresponding bounds on R are shown in Fig. 13.

As a simple way of comparing theoretical and observed spectra, one can treat R in (6)-(8) as an adjustable parameter and determine its "experimental" value by fitting the theoretical spectrum to the experimental spectra obtained for each patch of the ocean surface. In order to eliminate the influence of the unknown energy and action spectral fluxes, Q and P, anti obviate a difficult question about the specific values of the proportionality coefficients α and E, we shall use spectra in the normalized form (9). Ultimately, the values of R inferred by this analysis will be compared to the actual baroclinic Rossby radius of deformation known from *in situ* measurements.

As a measure of the distance between theoretical and experimental spectra we employ:

$$\Lambda(R, \nu) = \int_{K_a}^{K_b} [\tilde{F}_1^{theor}(k) - \tilde{F}_1^{exper}(k)]^2 \, dk \qquad (19)$$

where the tilde over F_1 points to the use of normalized spectra. The upper limit is set to Kb = 3/R to reduce the influence of irrelevant small-scale processes ("noises"). Selection of the lower limit depends on our choice of the spectral model. To employ the direct cascade model (7), we select K_a= 1/R. This choice minimizes the influence of the inverse cascade range which may be present at k < K_a. If the spectrum is assumed to be dominated by the inverse cascade at all wavenumbers below Kb, the lower limit of integration should include large scales; hence we choose K_a=0.4/R. This is the lowest wavenumber for which an experimental spectrum is deemed to be reliable: at wavenumbers below this limit, the estimates are distorted due to the limited size of an ocean area (10 by 10 degree) under consideration (GFG'96). The fact that both the integration limits and the spectrum $\tilde{F}_1^{theor}$ depend on an unknown parameter R complicate the numerical integration.

If the wave turbulence is weak (hence, v = 4), the problem reduces to minimizing the 1 D function A(R). An example of Δ(R) is provided in Fig. 14. In general, for an arbitrary degree of wave nonlinearity, v should be treated as an unknown parameter in the direct cascade range. The simplest method of minimizing (19) in this case is to estimate Δ(R,v) on a grid of R and v values and then find a point at which A attains its minimum. All such calculations have been conducted for 55 patches in the Atlantic.. Figure 15 illustrates the results for v based on the direct cascade model (7).

In order to check which IG WT model fits the observed spectra best, we conducted calculations separately - using the direct cascade model (7) for the high-wavenumber range and the inverse cascade model (8) for a much broader range of wavenumbers. This experiment showed that the direct cascade model yields best results for tropical latitudes, while the inverse cascade model best agrees with observations at latitudes greater than 20 degree. Consequently, the values of R used in Figs. 13 and 16 are based on two different models: in the renal bands right outside the equatorial waveguide, R has been determined based on (7). At all other latitudes we used (8). Using (7) for mid-latitudes yields, on the average, 25 percent greater values of K than those presented in Figs. 13 and 15. Using (8) for tropical regions leads to an average underestimation of R by about 25 percent. The limited success of the direct cascade model is probably due to the fact that most of the high-wavenumber range of observed spectra is dominated by noise. The appropriate model for this situation is illustrated in Fig. 6.

Unfortunately, not all of the spectra in Fig. 12 permit positive determination of R: the IG energy level in some regions is near the measuring noise level ($F(k) < 10^3$ cm^3/cpkm) and some spectra are apparently dominated by factors other than IG WT - their shape does not fit any simple description suggested either by IG WT or by 2D quasi-geostrophic turbulence theory. Such cases are discarded from further analysis and the corresponding patches in Figs. 15 and 16 are left blank. The equatorial region is excluded because the theory presented in Sect. 2 does not apply to (essential y 1 D) equatoriall y-trapped waves. Discussion of the results for the Atlantic is given in the next Section.

7. Application to the Atlantic **Ocean**

Atlantic ocean offers the full range of external conditions to be found in other regions of the World Ocean. We extracted from the T/P Geophysical Data Records (GDR) observations for cycles 15 through 68 covering 540 days of the T/P mission. The preparation of T/P data and details of its statistical analysis are described in GFG'96. The calculations have been carried out for 55 patches, each 10 by 10 degree in size, in the Atlantic ocean. The mean latitudes of the 10 by 10 degree patches in North Atlantic were set at 15, 25, 35, 45 and 55 degree N. For the South Atlantic we chose central latitudes at 10, 20, 30, 40 and 50 degree S.

7.1 Field of baroclinic IG WT

The amplitude of fast SSH variations, $W_0^{1/2}$, based on $W_{fast}(r)$ is shown in Fig. 11. The 1D spectra, $F_{fast}(k)$, of fast motions for the North and South Atlantic are illustrated in Fig. 12 separately. Since in most cases the observed spectra agree with (7) and (8), we interpret $W_0^{1/2}$ as the characteristic amplitude of baroclinic IG waves, and denote it by σ_{IG}. "l'he highest energy of JG WT is observed in the Gulf Stream region where IG waves are likely to be generated by the baroclinic instability of the vertical, quasi-geostrophic motions with respect to gravity mode perturbations. This supposition finds further confirmation in the South Atlantic where a relatively high level of IG WI’ is observed around the 30°’ latitude westward of 20^0W. This area is characterized by a very large meridional shear of the mean currents due to the passage of the Antarctic Circumpolar Current (ACC) and the convergence of the Brazil and Falkland currents in the western end. The highest amplitude of IG waves is observed at the southern tip of Africa where the powerful Aghulas current generates north-west-propagating eddies and, as we anticipate, radiates IG waves. Since the baroclinic Rossby radius (Fig. 16) derived for these regions takes on reasonable values (as compared to in situ measurements), we believe that the observed spectra of the fast motions are dominated by IG WT rather than by the fast moving eddies. The relevance of IG WT in such regions is further confirmed by the increased values of v (see Fig. 15) which correlate with the increased amplitude of fast motions. The lowest amplitude of IG waves is observed in the tropical region of the. South Atlantic. The characteristic values of σ_{IG} in the regions away from strong currents vary between 4 and 6 cm, corresponding to about 50 m for the amplitude of the thermocline depth oscillations.

Figure 16 provides a crude map of the 1st baroclinic Rossby radius inferred as explained in Sect. 6. Averaging this radius within zonal bands yields the latitudinal dependence of R, Fig. 13. We find that, while our inferred R exhibits the correct trend (decreasing poleward as - I/sin(O)), its values tend to be larger than the *in situ* results (triangles in Fig. 13) of Emery et al. (1984) and Houry et al. (1987). This discrepancy may be caused by over-simplifications of the present theory of IG WT - as discussed in (Glazman, 1996) and/or by various shortcomings of our data analysis technique.

Furthermore, the present poor understanding of the driving mechanism of IG WT does not allow us to specify the boundaries of the direct and inverse cascade ranges. As a result, in place of a composite spectrum containing both branches [introduced in (Glazman, 1996)], we had to employ in Sect.6 “partial” spectral models appropriate only within limited wavenumber subranges.

7.2 *Quasigeostrophic motion*

As suggested in Sect. *7.1,* baroclinic IG WT may receive, at least part of, its energy from the vertical component of oceanic motions, This suggestion finds an indirect confirmation in the our work,

In Fig. 17 we present the characteristic amplitude, $W_0^{1/2}$, of the slow motions dominated by baroclinic Rossby waves, In the vicinity of the Gulf Stream, ACC, and Aghulas Current systems, the amplitude of the slow motions is, of course, at its highest; while in the subtropics and other regions away from strong currents, the amplitude is vanishingly small. These spatial variations of W_0 tend to correlate with variations of the IG WT amplitude in Fig. 11, and with the degree of the IG wave nonlinearity quantified by v in Fig. 15. This leads to a conjecture that at least one of the sources of baroclinic IG wave energy is the 2D quasi-geostrophic turbulence attaining its highest levels in the regions of large lateral shear of the ocean current velocity. The closest analog for this mechanism is the well known generation of acoustic pressure waves by the 3D turbulence. The divergence of the horizontal velocity field causing thermocline depth oscillations in the case of IG waves is similar to the divergence (at sufficiently high frequencies) of the 3D velocity field causing sound waves.

The fact that the IG WT amplitude remains finite in many regions where the amplitude of the slow motions is vanishingly small (e.g., in the zonal band centered at 20^0S) points to the presence of other possible sources of IG WT energy - not related to the 2D vortical motion. The scattering of barotropic tides on ocean floor features has long been viewed as a natural mechanism of baroclinic wave generation. Many spectra in Fig. 12 contain a little bump (or other kind of irregularity) at wavenumbers corresponding to the barotropc tide frequency - as predicted by eq.(2) and illustrated by boxes at the curves of Figs. 1-6. This feature of wave spectra maybe associated with the tidal forcing. While we cannot presently assess the contribution of the tidal mechanism to baroclinic IG wave energy, we remind the reader that the estimates of the Kolmogorov constant, α_q, and spectral flux Q presented in Sect. 2.2 are consistent with our suggestion that a portion of Q may be contributed by barotropic tide.

8. **Summary and Conclusions**

Our analysis of the SSH field in the Atlantic has demonstrated that the fast component of SSH variations (with the characteristic timescale under 1 day) makes a substantial contribution to the total SSH variability. Its amplitude on the average is about 5 cm, and in some regions it exceeds 15 cm. These fast SSH oscillations are characterized by wavenumber spectra whose shape and dependence on external factors (the first baroclinic Rossby radius of deformation) are in good agreement with theoretical predictions for baroclinic IG WT. We thus conclude that the fast component of the observed SSH signal represents surface manifestation of long nonlinear internal waves of the first baroclinic mode. The degree of these waves' nonlinearity is low for most of the Atlantic. However, in regions of an intense generation of baroclinic IG WI' - where their amplitude is well above the average - the wave nonlinearity tends to be high, attaining the regime of saturated spectrum F_1 I(k) - k^{-5} in some of the regions.

The high-wavenumber range of altimeter-measured SSH spectra - atk20.008 cpkm - is dominated by intervening factors, such as altimeter measuring errors. The effect of such factors is well represented by a simple model of shot noise, F_1(k) ≈ Ilk-1. The noise obscures manifestations of the direct energy cascade in the high-wavenumber range of the spectra, thus reducing usefulness of our equation (7) for describing the observations. At wavenumbers below k ≈ 0.007 cpkm, the observed spectra are best represented by the theoretical model for the inverse cascade range.

The large-scale quasi-geostrophic motions are dominated by baroclinic Rossby waves. In regions of strongly sheared mean currents (Gulf Stream, Aghulas current, ACC), this component of the SS11 field attains its highest amplitude. The observed correlation between the high amplitude of slow motions and the high amplitude of IG WT points to the important role played by the vertical oceanic motions in the generation of baroclinic IG waves. Analogy with the generation of acoustic waves by the classical 3D turbulence is rather transparent.

Barotropic tides scattered by ocean floor topography are pointed out as an additional source of baroclinic wave energy. In regions away from major ocean current systems, this mechanism may become dominant. The fact that the inertial cascade of wave energy in baroclinic IG waves implies eventual dissipation of energy in the small-scale range of the spectrum points to baroclinic IG WT as a factor of global dissipation of ocean tides.

Baroclinic Rossby waves are characterized by a wide range of scales and propagation directions. While the zonal component of the wave velocity vector is predominantly westward (except for the ACC region where the waves are advected eastward by the mean ocean current), the meridional component varies strongly and usually is greater than the zonal component. In other words, the mean direction of Rossby wave propagation is far from zonal. Therefore, the conventional view of Rossby waves as being generated at eastern boundaries of ocean basins and then propagating across the basin to reach the western boundary is in strong disagreement with our results.

ACKNOWLEDGMENTS: This work was performed at the Jet Propulsion Laboratory, California Institute of Technology, under contract with the National Aeronautics and Space Administration. The financial support provided for Dr. B. Cheng by the Office of Naval Research is also gratefully acknowledged.

CAPTIONS FOR FIGURES

Figure 1. 1 D spectrum, $F_1(k)=\varepsilon kF(k)$, of SSH spatial variations due to weak baroclinic IG wave turbulence dominated by the direct energy cascade. Here, E = 10–6, and F(k) is based on (6) with $\alpha = 10$, $H_1=500$ m, and c = 2.5 m/s. Solid curve: $\Theta=20$ deg, R=45 km. Dotted curve: $\Theta=35$ deg, R=27 km. Dashed curve: $\Theta=50$ deg, R=20 km. Dash-dot curves provide power laws for reference. Boxes at the curves designate wavenumber k_T.

Figure 2. 1 D spectrum, $F_1(k)$, of SSH spatial variations due to strong baroclinic IG wave turbulence ($\nu= 10$) dominated by the direct energy cascade. F(k) is based on (7) with $\alpha_{10}Q$’9 ≈.O 02 Other notations are as in Fig.1.

Figure 3. 1D spectrum, $F_1(k)$, of SSH spatial variations due to baroclinic IG wave turbulence dominated by the inverse cascade of wave action: F(k) is based on (7) with same parameters as used for Fig. 1. Other notations are also as in Fig. 1

Figure 4. Non-dimensional 1D spectrum $\tilde{F}_1(k)$ of SSH spatial variations due to weak baroclinic IG wave turbulence dominated by the direct energy cascade. Based on (6) and (8) with the same parameters and notations as in Fig. 1.

Figure 5, Non-dimensional 1D spectrum $\tilde{F}_1(k)$ of SSH spatial variations due to weak baroclinic IG wave turbulence dominated by the inverse cascade of wave action. Based on (7) and (8), with the same parameters ancl notations as in Fig. 1.

Figure 6. 1D spectrum, $F_1(k)$, of SSH spatial variations due to weak baroclinic IG wave turbulence dominated by the inverse cascade of wave action, in the presence of error noise. Based on (7) and (9), with the same parameters and notations as in Fig. 1.

Figure 7. Three sections of the autocorrelation function $W(\mathbf{r},\tau)$ for a 10 by 10 deg area of the South Atlantic centered at 30°S, 5^0E.

Top panel: $W(r_x,0,\tau)$. Middle panel: $W(0,r_y,\tau)$. Bottom panel: $W(r_x,r_y,0)$.

Figure 8. The same as Fig. 7 but for a 10 by 10 deg area of the South Atlantic centered at 30%, 25^0W.

Figure 9. Estimation of IG wave spectra for a 10 by 10 degree patch centered at 30°S and 5^0E (in correspondence with Fig.7):

Panel A: 1D autocorrelation functions: Solid curve: W(r) given by eq.(12) for along-track SSH variations, Dotted curve: $W_{slow}(r)$ obtained from $W_{slow}(\mathbf{r})$ by angular integration (13). Dashed curve: $W_{fast}(r) = W(r) - W_{slow}(r)$. Black circle: σ^2_{IG} found as W_0 in (15) for $W_{fast}(r)$.

Panel B: 1D spectra corresponding to 1D autocorrelation functions in Panel A.

Figure 10. The same as Fig.9, but for the surface patch centered at 30°S and 25°W (in correspondence with Fig.8).

Figure 11. Square root, σ_{IG}, of the SSH variance component due to fast motions, estimated as $W_0^{1/2}$ in (15) based on $W_{fast}(r)$. This quantity is interpreted as the characteristic surface amplitude of baroclinic IG waves.

Figure 12. 1D spectra of baroclinic IGWT obtained based on T/P altimeter data as explained in Sect. 4.2. Panel A: North Atlantic. Panel B: South Atlantic. The units, scale and range of the vertical and horizontal axes are the same as in Panel B of Figs. 9 and 10. The lon and lat coordinates of a patch are provided on top of each plot.

Figure 13. First internal Rossby radius of deformation averaged within zonal bands and referenced to geographic latitude. Triangles: based on analysis of the observed density stratification by Emery et al. (1984) and Houry et al. (1987). Solid curve: based on eqs. (3) and (4) with h = 0.5 m. Dashed curve: based on eqs. (2) and (3) with h = 1.0 m. Solid dots: inferred from T/P altimeter measurements as explained in Sect. 6.

Figure 14. Function A(R) defined by Eq. (19) for $\tilde{F}_1^{theor}$ dominated by the inverse cascade of wave action (8). Here we use the experimental spectrum $\tilde{F}_1^{exper}$ for a surface patch centered at 15^{0}W, 20°S.

Figure 15. The effective number, v, of resonantly interacting wave harmonics derived from the spectra of Fig. 10 as explained in Sect. 6.

Figure 16. The baroclinic Rossby radius of deformation derived from the spectra of Fig. 12 as explained in Sect. 6.

Figure 17. The characteristic amplitude of quasi-geostrophic motions, $W_0^{1/2}$, derived based on $W_{fast}(r)$ as explained in Sect. 4.

REFERENCES

Baines, P. G., 1982. On internal tide generation models. Deep-Sea Res., 29 (3A), 307-338.

Branger, H., A. Ramamonjiarisoa, and L. F. Bliven, 1993. AKu-band laboratory experiment on the electromagnetic bias. IEEE Trans. Geosci. hem. Sens., 31(6), 1165-1179.

Cox, C.S. and H. Sandstrom, 1962, Coupling of internal and surface waves in water of variable depth. J. Ocean. Sot. Japan, 20th Ann vol., 499-513.

Chelton, D.B. and M. G. Schlax, 1996, Global observations of oceanic Rossby waves. Science, **272, 234-238.**

Desaubies, Y.J.F. 19"/3, Internal waves near the turning point. Geophys. Fluid Dyn., 5, 143-154,.

Emery, W. J., W.G. lee, and L. Magaard, 1984, Geographic and seasonal distributions of Brunt-Väisälä frequency and Rossby radii in the North Pacific and North Atlantic. Journ. Phys. Oceanogr., 14, 294-317

Falkovich, G., 1992: Inverse cascade and wave condensate in mesoscale atmospheric turbulence. Phys. Rev. Lett., 69(22), 3173-3176.

Falkovich, G.E. and S.B. Medvedev, 1992. Kolmogorov-like spectrum for turbulence of inertial-gravity waves. Europhys. Let. 19(4), 279-284.

Falkovich, G., A. Shafarenko, and G. Wilford, 1995. Join behavior of inertio-gravity and Rossby waves. Physica D, 87, 285-289.

Fu, L.L., E.J. Christensen, C.A. Yamarone Jr., M. Lefebvre, Y. Menard, M. Dorrer, and P. Escudier, 1994. TOPEX/POSEIDON mission overview. J. Geophys. Res., 99(C12), 24,369-24,381.

Gaspar, P. and C. Wunsch, 1989. Estimates from altimeter data of baroclinic Rossby waves in the Northwestern Atlantic Ocean. Jour. Phys. Oceanogr., 19, 1821-1844.

Glazman, R.E., 1993. A cascade model of wave turbulence with applications to surface gravity and capillary waves. Fractals, 1 (3), 513-520.

Glazman, R. E. 1995. A simple theory of capillary-gravity wave turbulence. J. Fluid Mech., vol. **293, 25-34.**

Glazman, R.E., 1996, Spectra of baroclinic inertia-gravity wave turbulence. Journ. Phys. Oceanogr. 26(7), 1256-1265.

Glazman, R. E. Scale-dependent ocean wave turbulence. In: "Stochastic Models in Geosystems," Eds.: S. A. Molchanov and W. A. Woyczyncki. IMA Volumes in Mathematics and its Applications, Vol. 85. pp.97- 114. Springer Verlag, New York. 1996.

Glazman, R.E., A. Fabrikant and A. Greysukh, 1996. Statistics of spatio-temporal variations of sea surface height based on Topex altimeter measurements. Int. J. Rem. Sensing, 17(13), 2647-2666.

Hasselmann, K., 1962, On the non-linear energy transfer in a gravity-wave spectrum. J. Fluid Mech., 12, 481-500.

Houry, S., E. Dombrowsky, P. De May, and J.F. Minster, 1987, Brunt-Väisälä frequency and Rossby radii in the South Atlantic. Journ. Phys. Oceanogr., 17, 1619-*1626.*

Larraza, A., S.L. Garrett, and S. Putterman, 1990. Dispersion relations for gravity waves in a deep fluid: Second sound in a stormy sea. Phys. Rev. A 41 (6), 3144-31 SS.

Le Traon, P.Y. 1992, Contribution of satellite altimetry to the observations of oceanic mesoscale variability. Oceanological Acts, 15(5), 441-457.

Le Traon, P. Y., M.C. Rouquet and C. Boissier. 1990, Spatial scales of mesoscale variability in the north Atlantic as deduced from Geosat data. J. Geophys. Res., 95(C1 1), 20,267-20,285.

Le Traon, P. Y., J. Stum, J. Dorandeu, and P. Gaspar, 1994. Global statistical analysis of Topex and Poseidon data. J. Geophys. Res., 99(C12), 24,619-24,631.

Munk, W. H., Abyssal recipes, Deep-Sea Res., 13, 707-730, 1966.

Munk, W. H. Internal wave. spectra at the buoyant and inertial frequencies. Journ. Phys. Oceanogr. 10, 1718-1728, 1980.

Pollard, R. T., 1970, On the generation by winds of inertial waves in the ocean. Deep-Sea Res., 17, 795-812.

Webster, F., 1968, Observations of inertial period motions in the deep sea, Rev. Geophys. Space Phys., 6, 473-490.

Zakharov, V.E., 1984. Kolmogorov spectra in weak turbulence problems. Handbook of Plasma Physics, Eds. M, N. Rosenbluth and R.Z. Sagdeev. Chapter 5.1. Elsevier Science Publishers, pp.4-36.

Zakharov, V. E. and M.M. Zaslavskii, 1982. The kinetic equation and Kolmogorov spectra in the weak turbulence theory of wind waves. Izvestiya, Atmospheric and Oceanic Physics (English Translation), 18(9), 747-753

Zakharov, V.E., V.S. L'vov and G. Falkovich. 1992. Kolmogorov Spectra of Turbulence I: Wave Turbulence. Springer Verlag, Berlin, 264 pp.

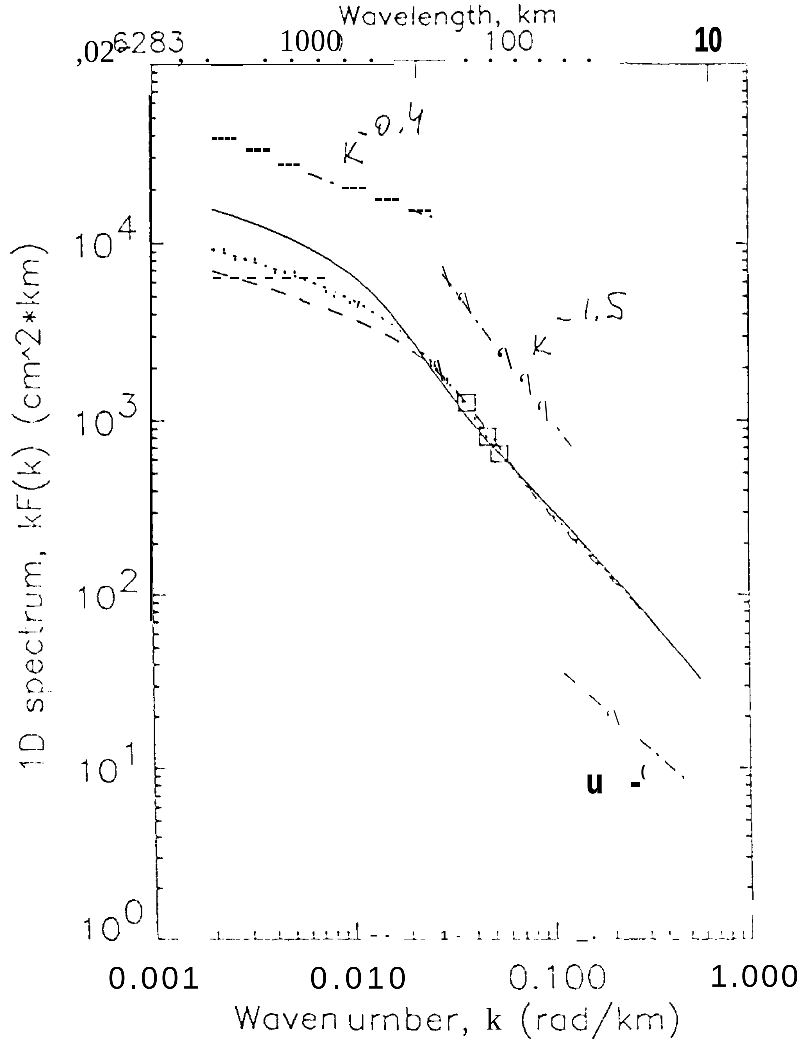
Wavelength, km
6283
1000
100
10
1D spectrum, kF(k) (cm^2*km)
10^4
10^3
10^2
10^1
10^0
$k^{-0.4}$
$k^{-1.5}$
0.001
0.010
0.100
1.000
Wavenumber, k (rad/km)

Fig. 1

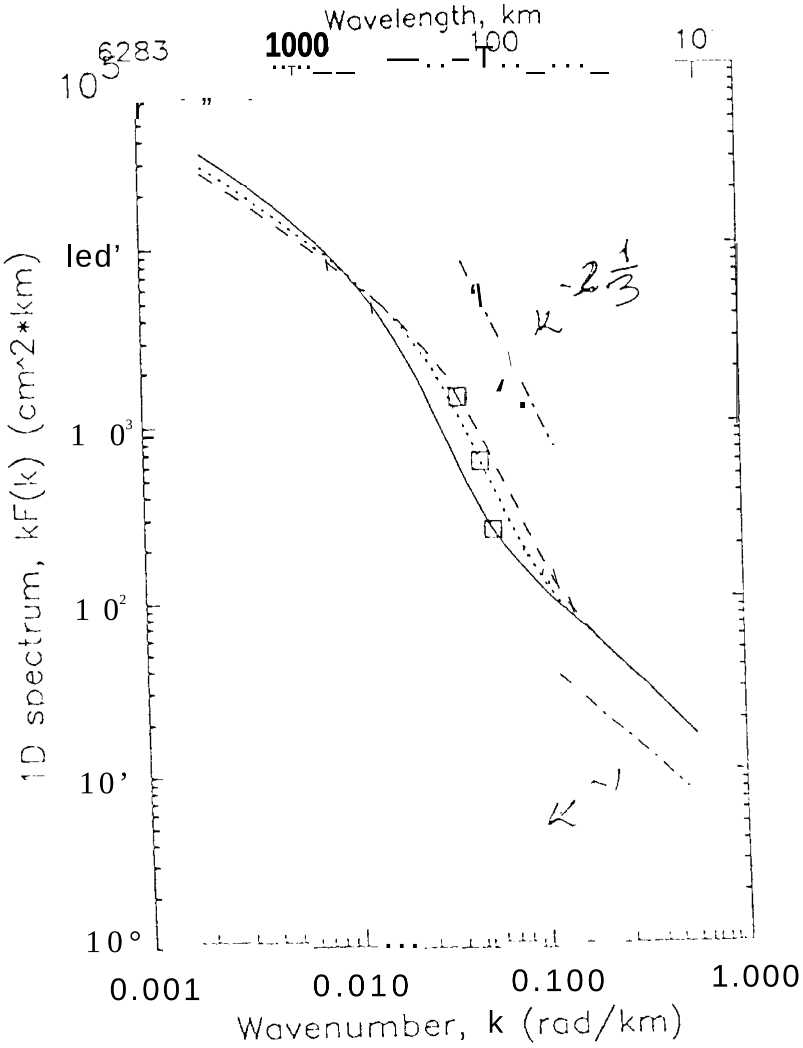
Wavelength, km
6283
1000
100
10
10^5
10^4
10^3
10^2
10^1
10^0
1D spectrum, kF(k) (cm^2*km)
$k^{-2\frac{1}{3}}$
k^{-1}
0.001
0.010
0.100
1.000
Wavenumber, k (rad/km)

Fig. 2

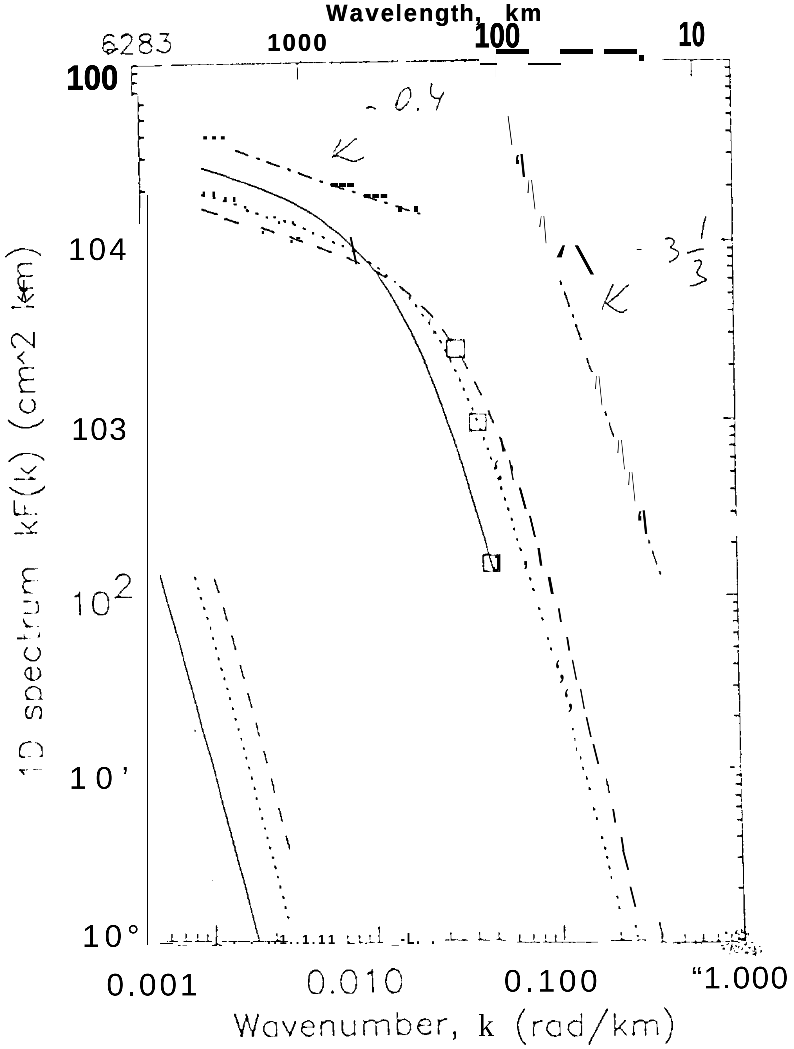
Wavelength, km
6283
1000
100
10
100
104
103
10^2
10'
10°
0.001
0.010
0.100
"1.000
Wavenumber, k (rad/km)
1D spectrum kF(k) (cm^2 km)
-0.4
-3 1/3

Fig. 3

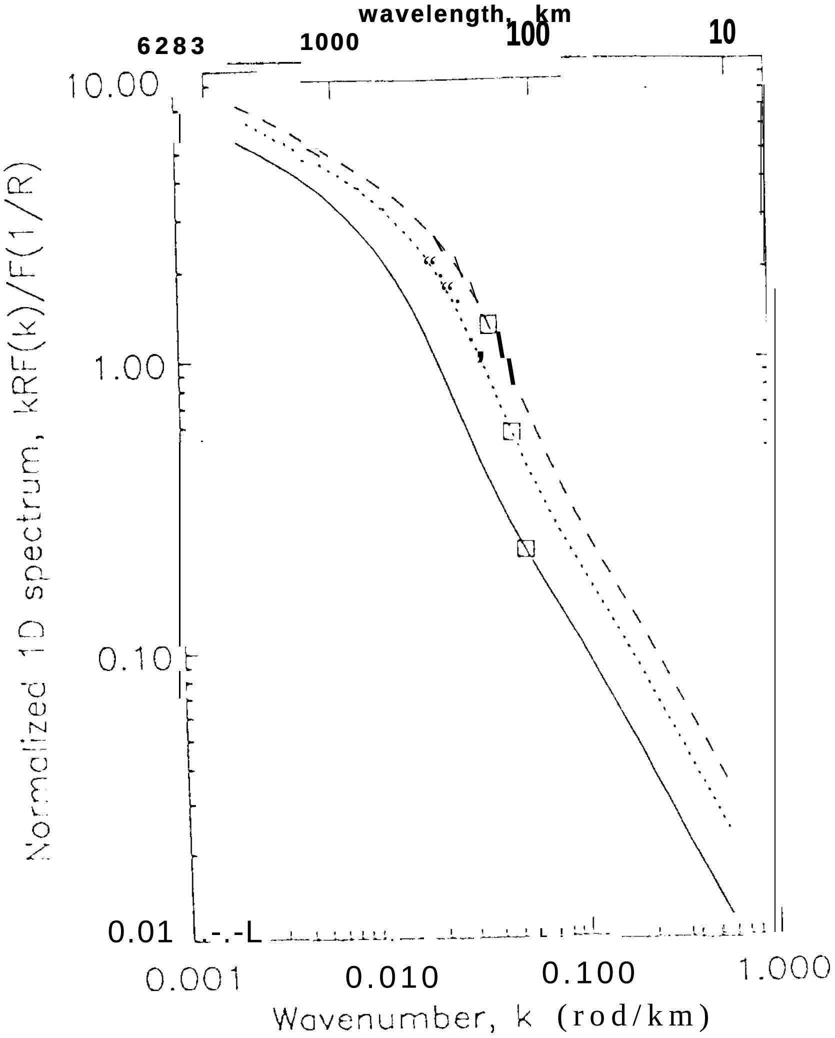
wavelength, km
6283
1000
100
10
10.00
1.00
0.10
0.01
0.001
0.010
0.100
1.000
Wavenumber, k (rod/km)
Normalized 1D spectrum, kRF(k)/F(1/R)

Fig. 4

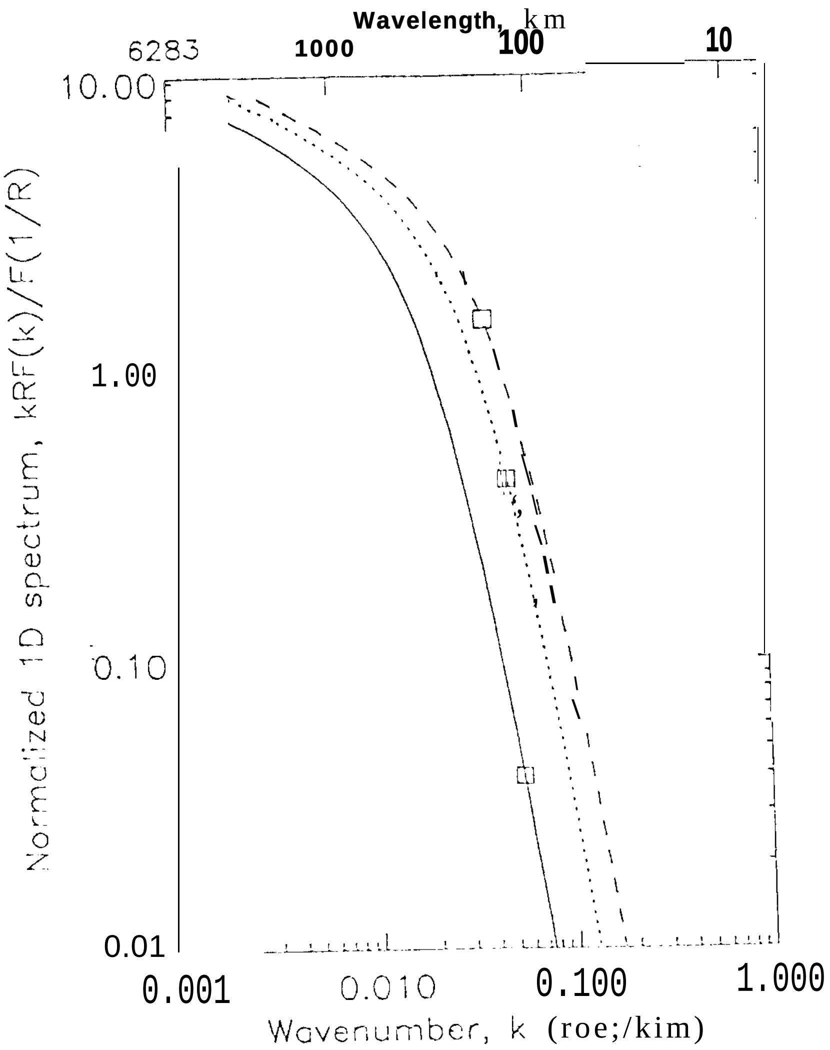
Wavelength, km
6283
1000
100
10
10.00
1.00
0.10
0.01
Normalized 1D spectrum, kRF(k)/F(1/R)
0.001
0.010
0.100
1.000
Wavenumber, k (roe;/kim)

Fig. 5

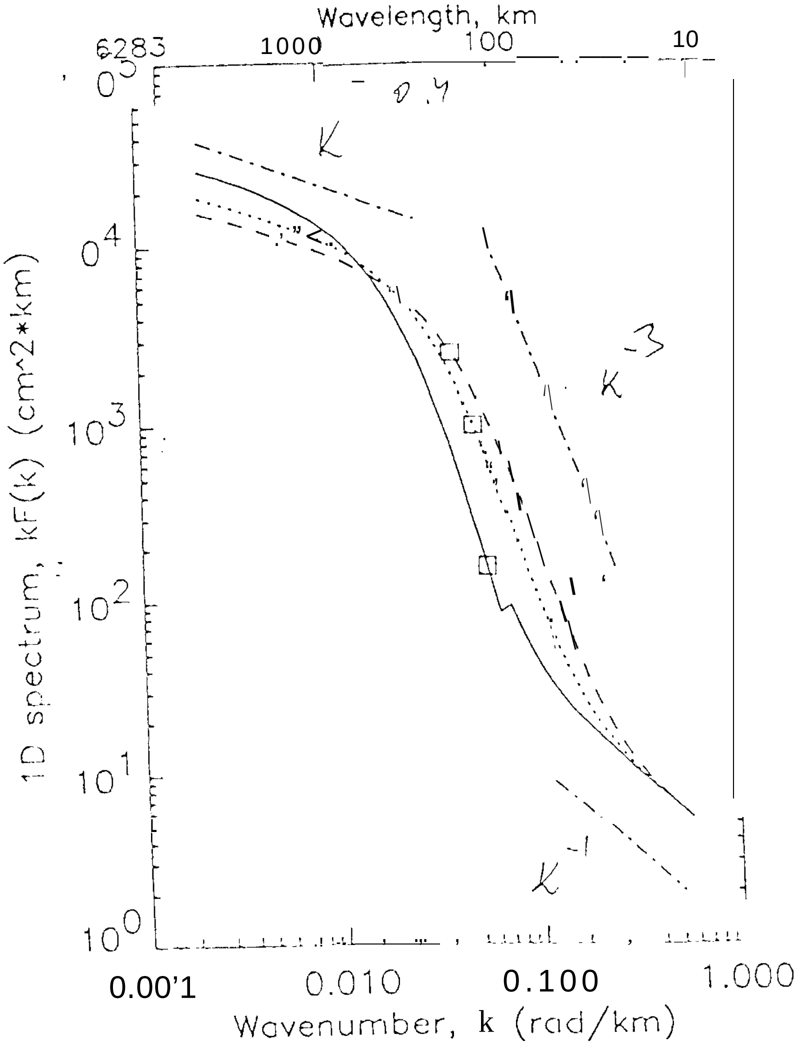
Wavelength, km
6283
1000
100
10
0^5
k
0^4
k^{-3}
10^3
10^2
10^1
k^{-1}
10^0
1D spectrum, kF(k) (cm^2*km)
0.00'1
0.010
0.100
1.000
Wavenumber, k (rad/km)

Fig. 6

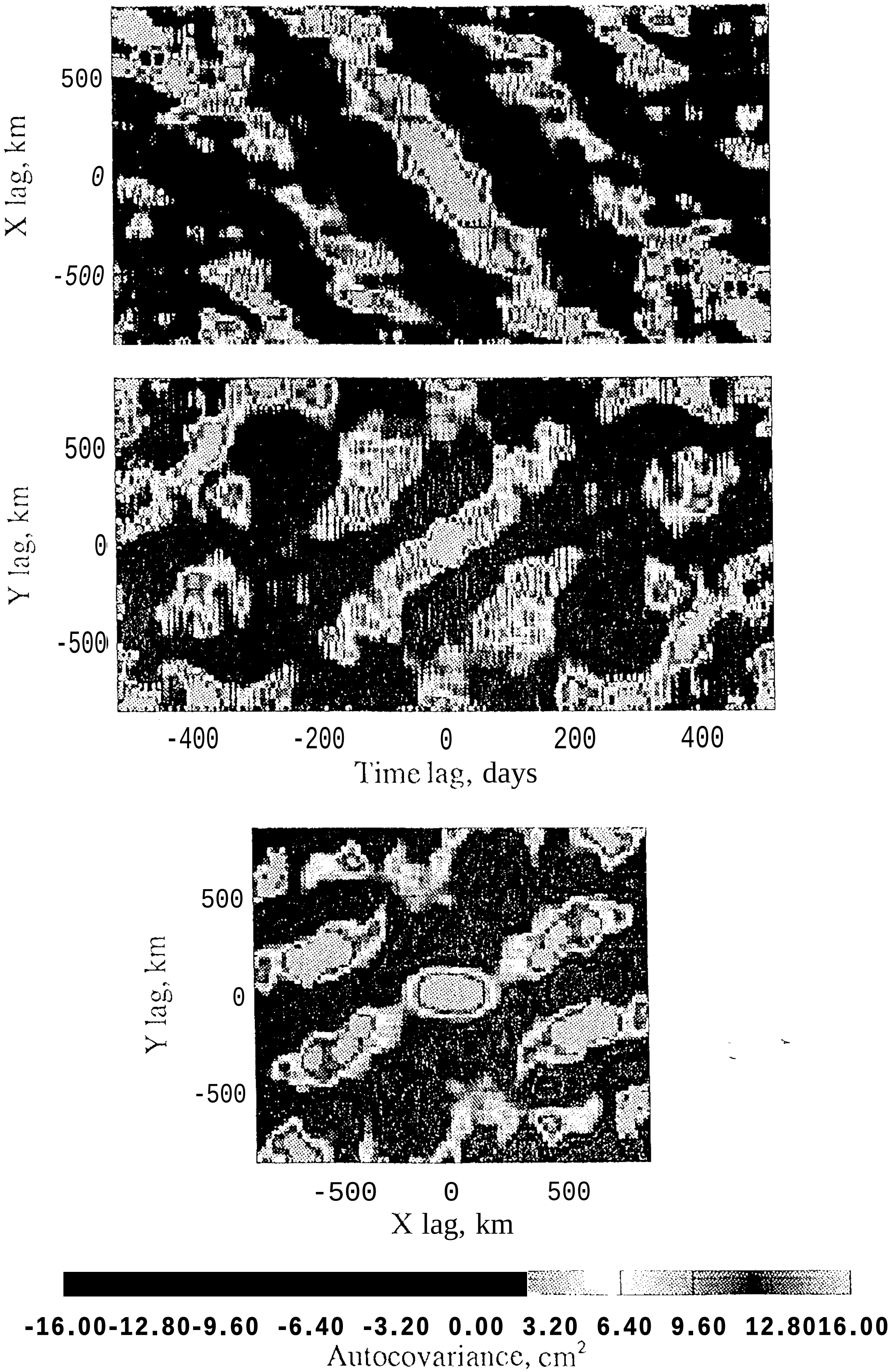
500
0
-500
X lag, km
500
0
-500
Y lag, km
-400
-200
0
200
400
Time lag, days
500
0
-500
Y lag, km
-500
0
500
X lag, km
-16.00
-12.80
-9.60
-6.40
-3.20
0.00
3.20
6.40
9.60
12.80
16.00
Autocovariance, cm^2

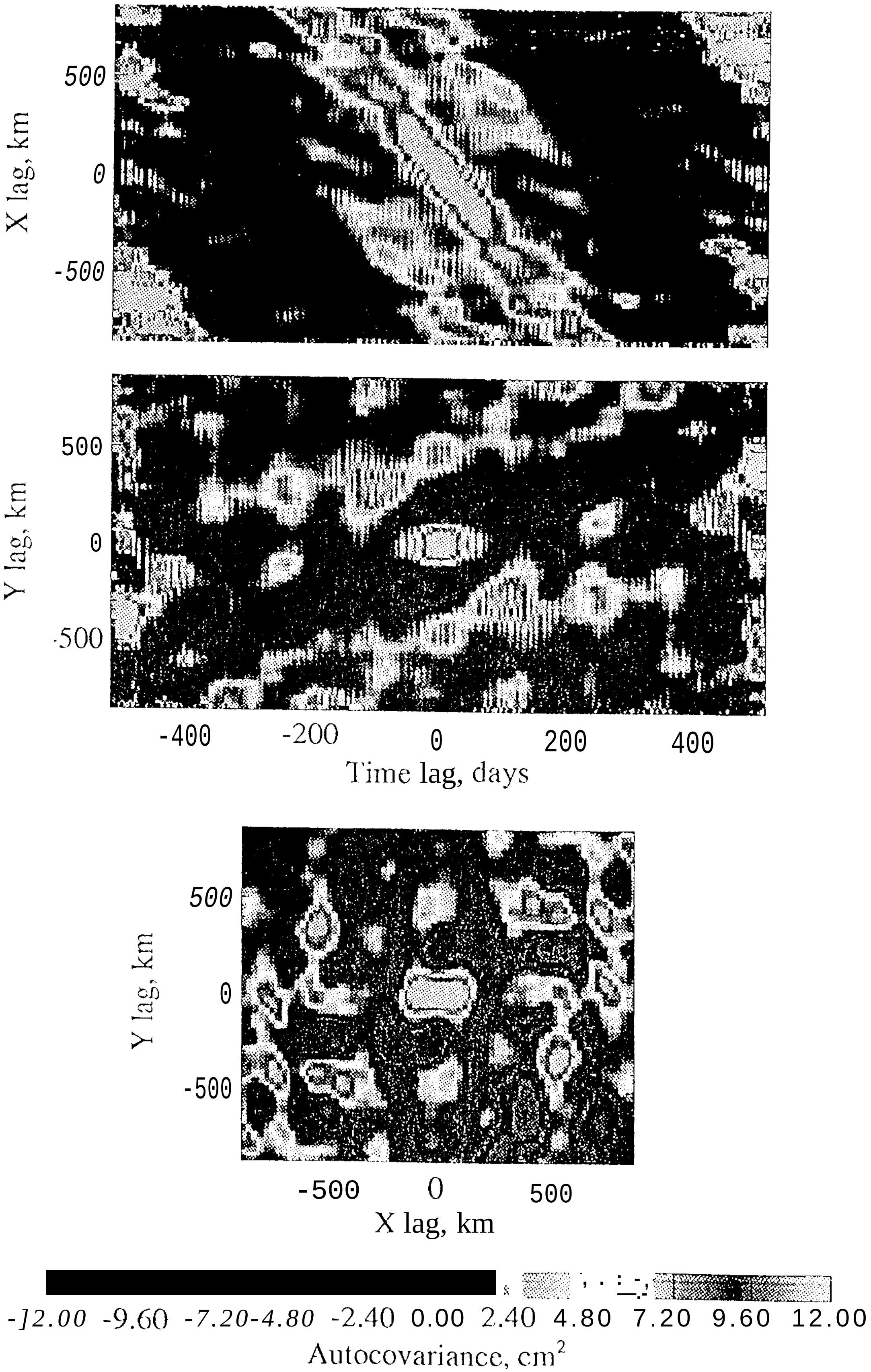
500
0
-500
X lag, km
500
0
-500
Y lag, km
-400
-200
0
200
400
Time lag, days
500
0
-500
Y lag, km
-500
0
500
X lag, km
-12.00
-9.60
-7.20
-4.80
-2.40
0.00
2.40
4.80
7.20
9.60
12.00
Autocovariance, cm²

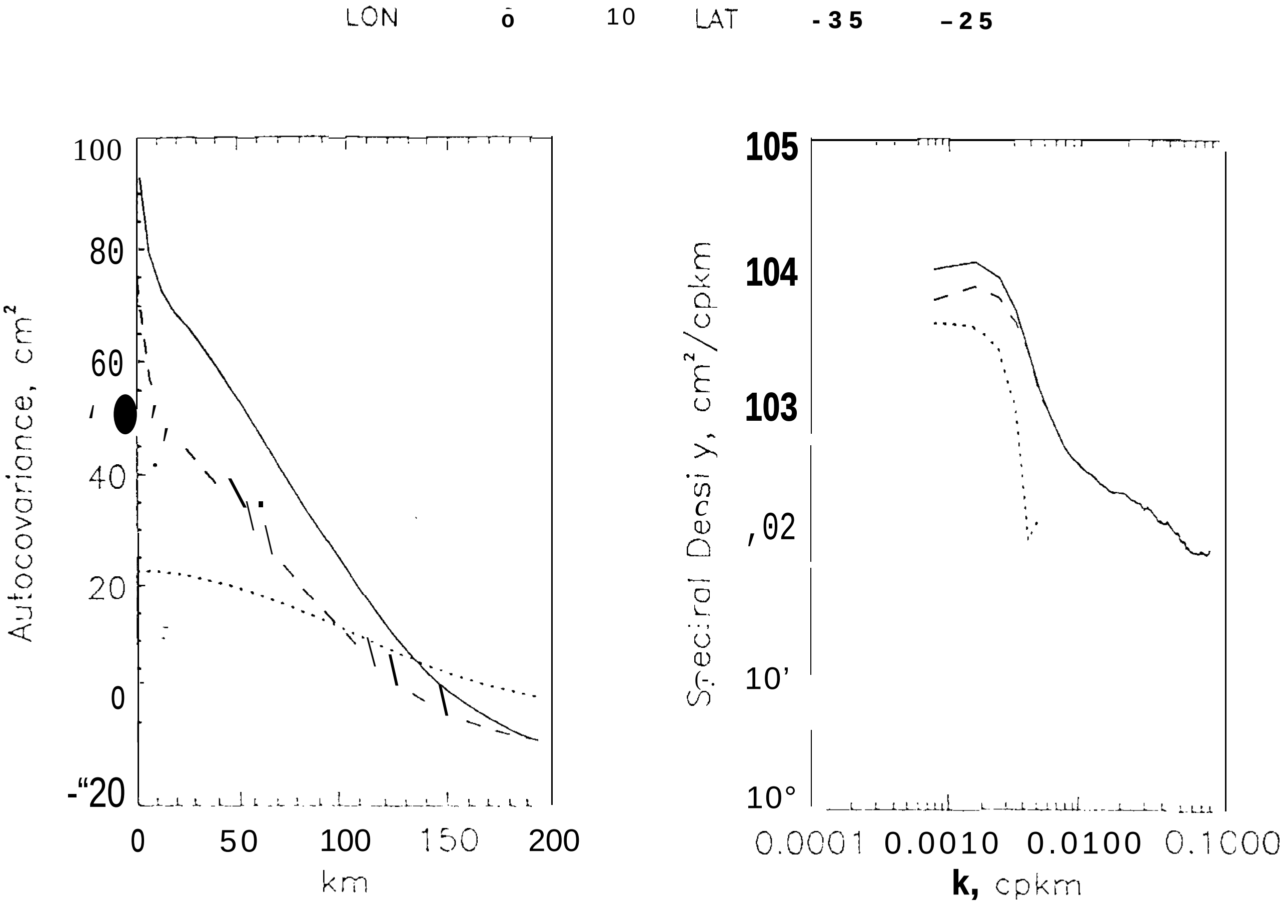
LON 0 10 LAT -35 -25
Autocovariance, cm²
100
80
60
40
20
0
-20
0
50
100
150
200
km
Spectral Density, cm²/cpkm
10⁵
10⁴
10³
10²
10¹
10⁰
0.0001
0.0010
0.0100
0.1000
k, cpkm

Fig. 9.

LON 330 340 LAT -25

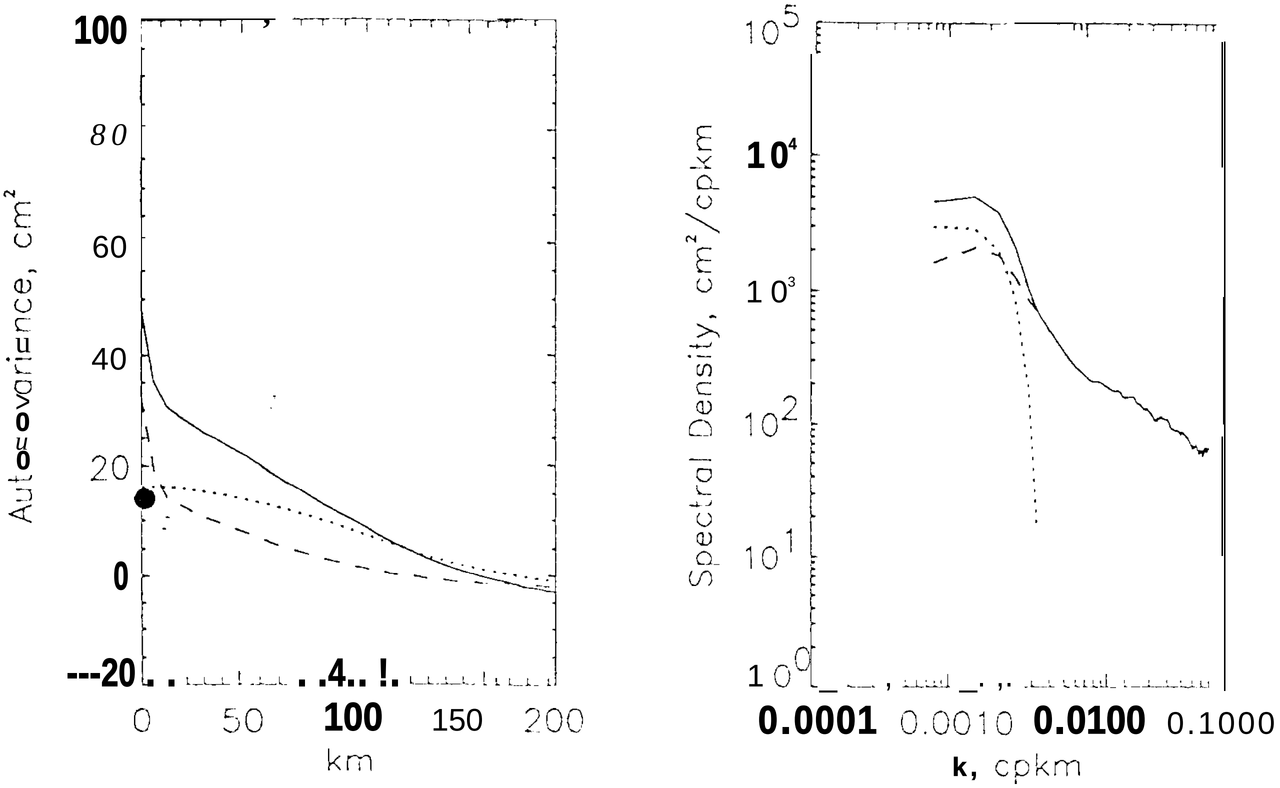

Along tracks

Fig. 10

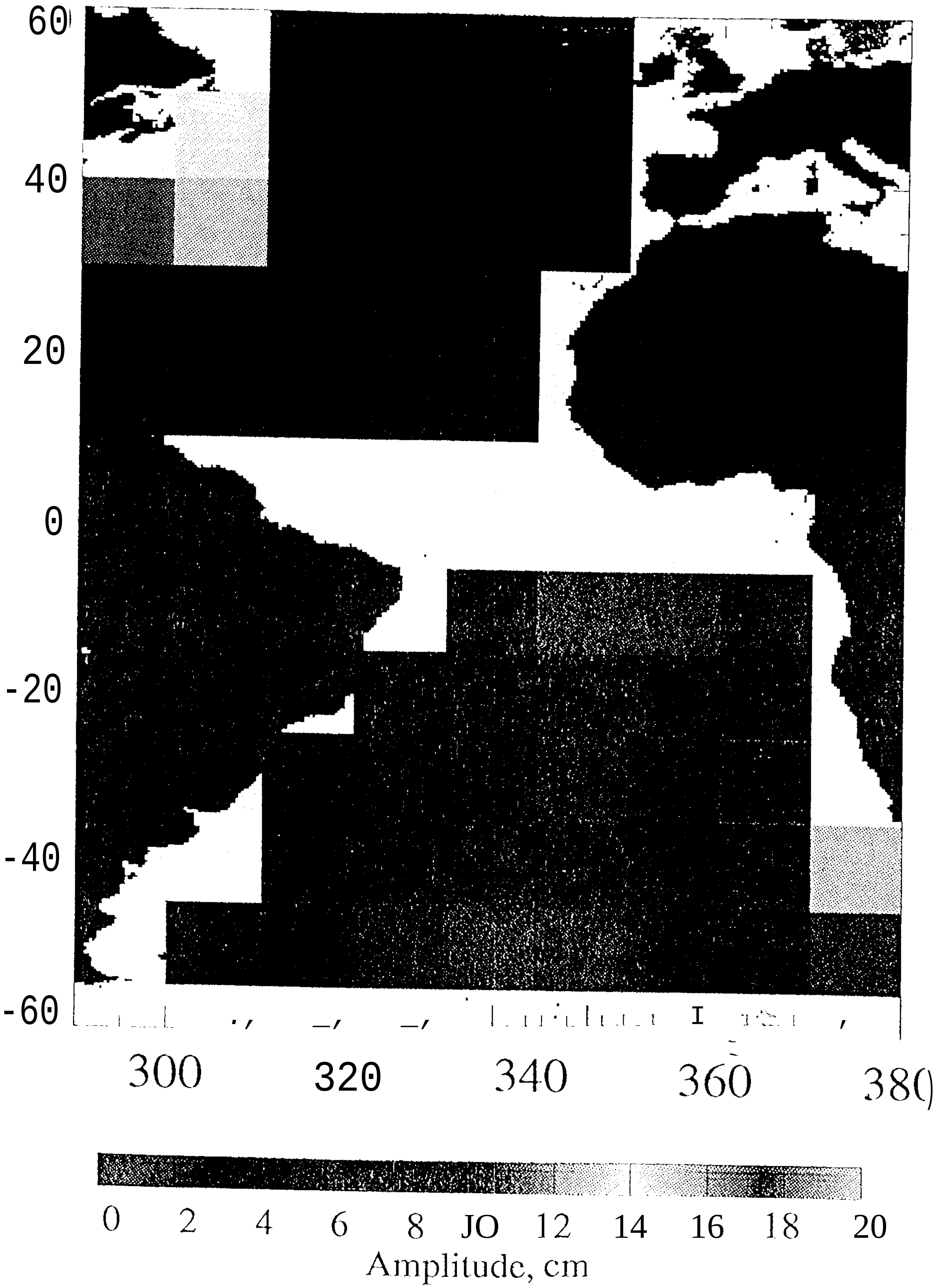
60
40
20
0
-20
-40
-60
300
320
340
360
380
0
2
4
6
8
10
12
14
16
18
20
Amplitude, cm

Fig. 12

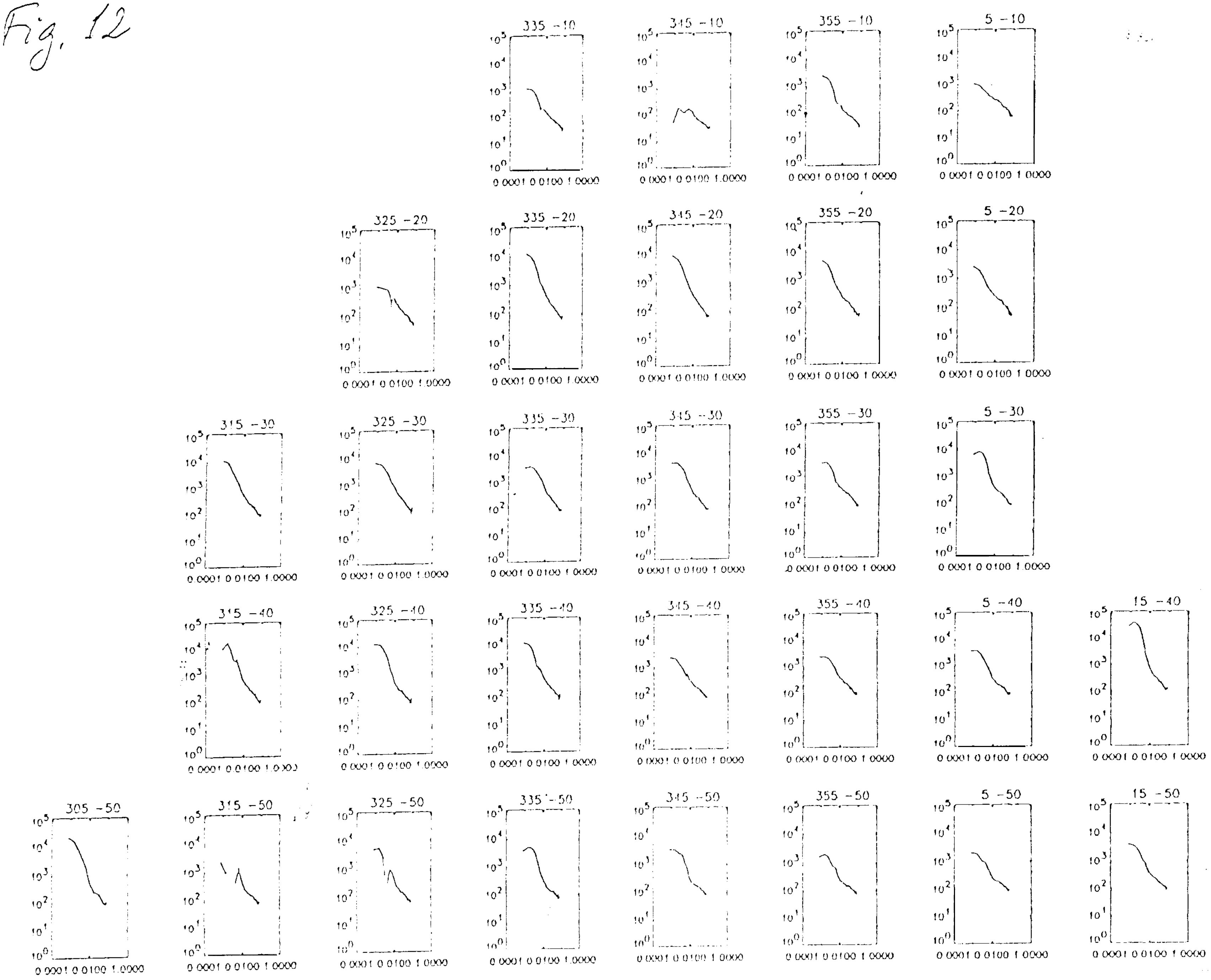
335 -10
345 -10
355 -10
5 -10
325 -20
335 -20
345 -20
355 -20
5 -20
315 -30
325 -30
335 -30
345 -30
355 -30
5 -30
315 -40
325 -40
335 -40
345 -40
355 -40
5 -40
15 -40
305 -50
315 -50
325 -50
335 -50
345 -50
355 -50
5 -50
15 -50
10^5
10^4
10^3
10^2
10^1
10^0
0.0001 0.0100 1.0000

Fig. 12
continued

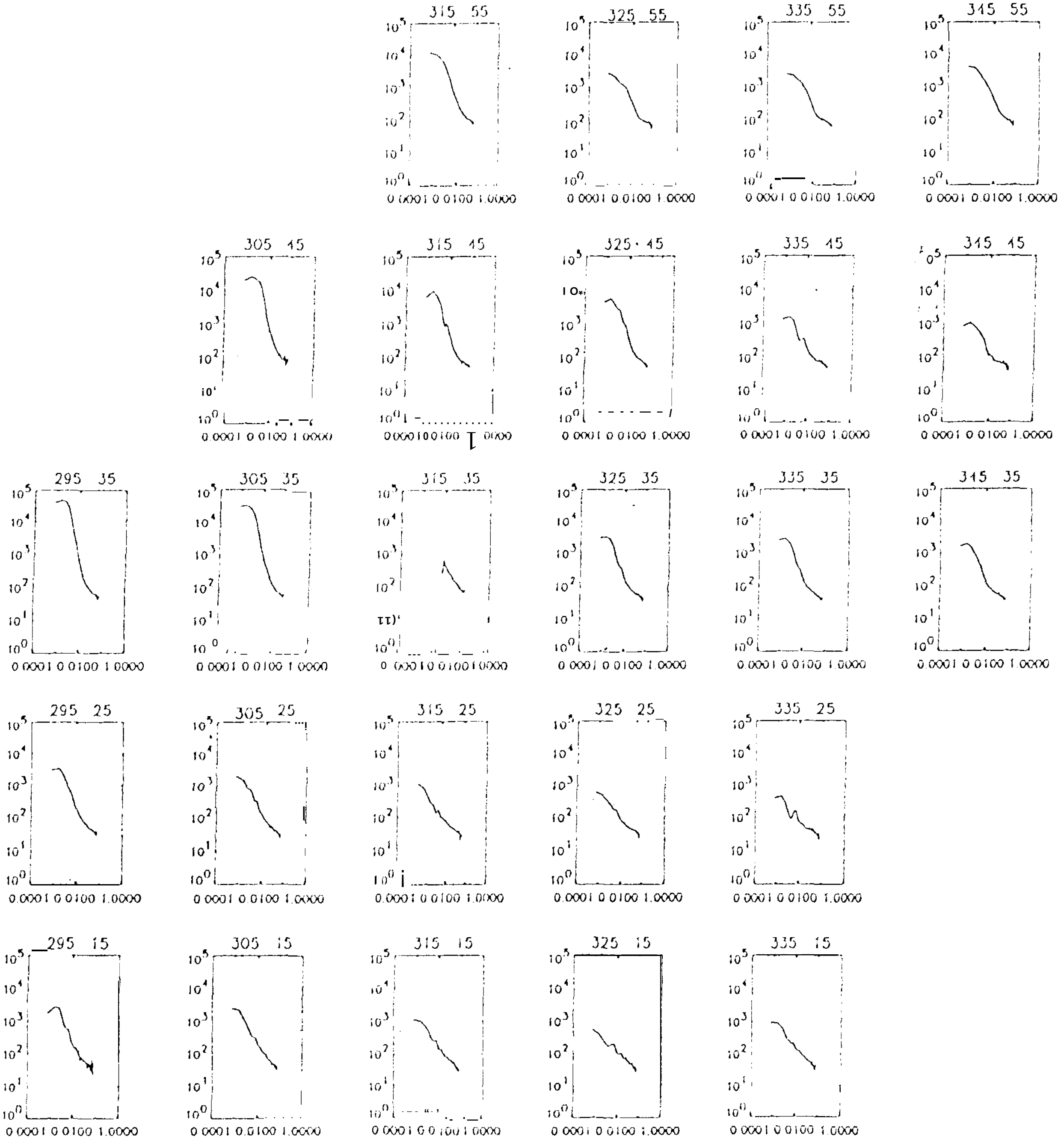

Fig. 12

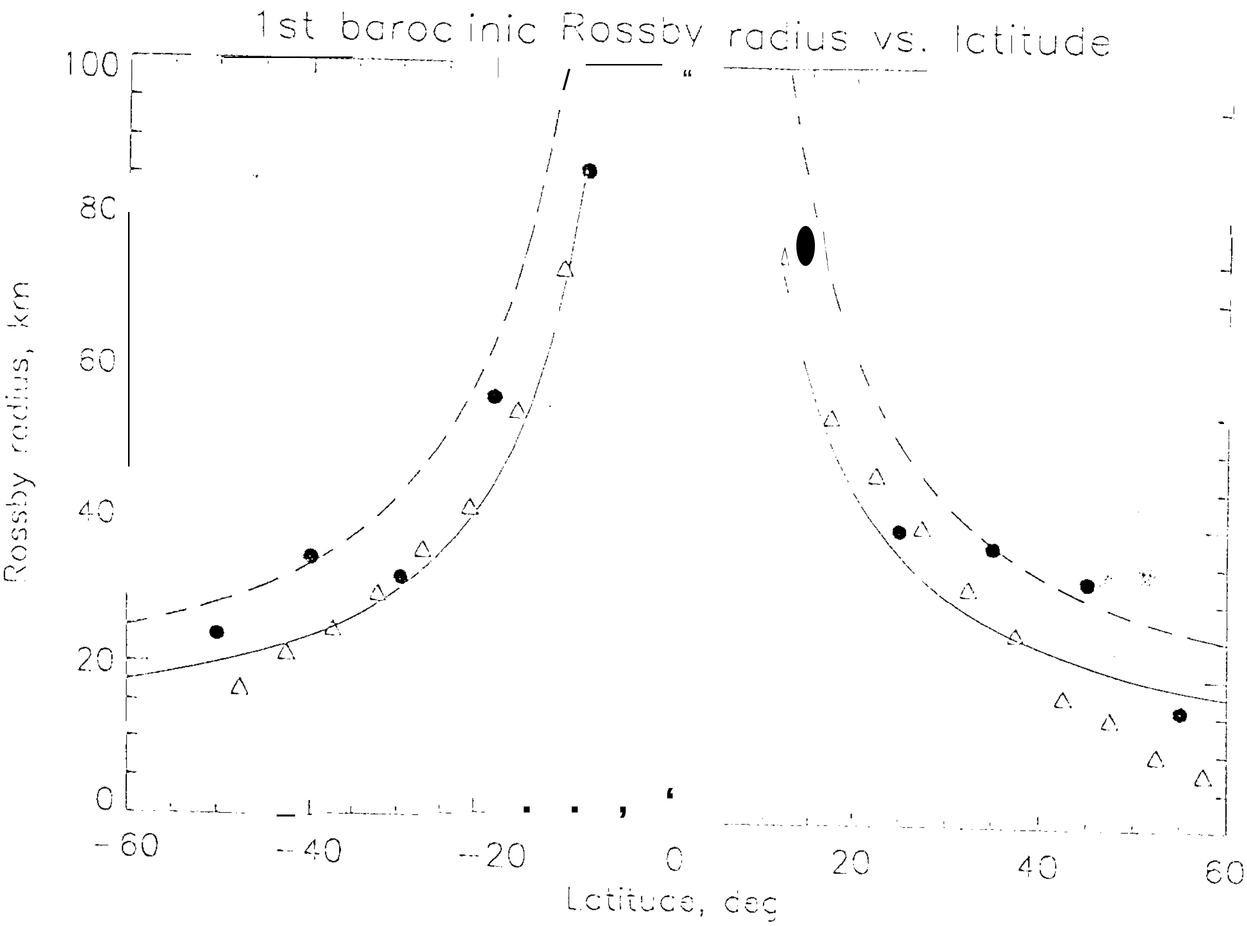

1st baroclinic Rossby radius vs. latitude
Rossby radius, km
100
80
60
40
20
0
-60
-40
-20
0
20
40
60
Latitude, deg

Fig. 13

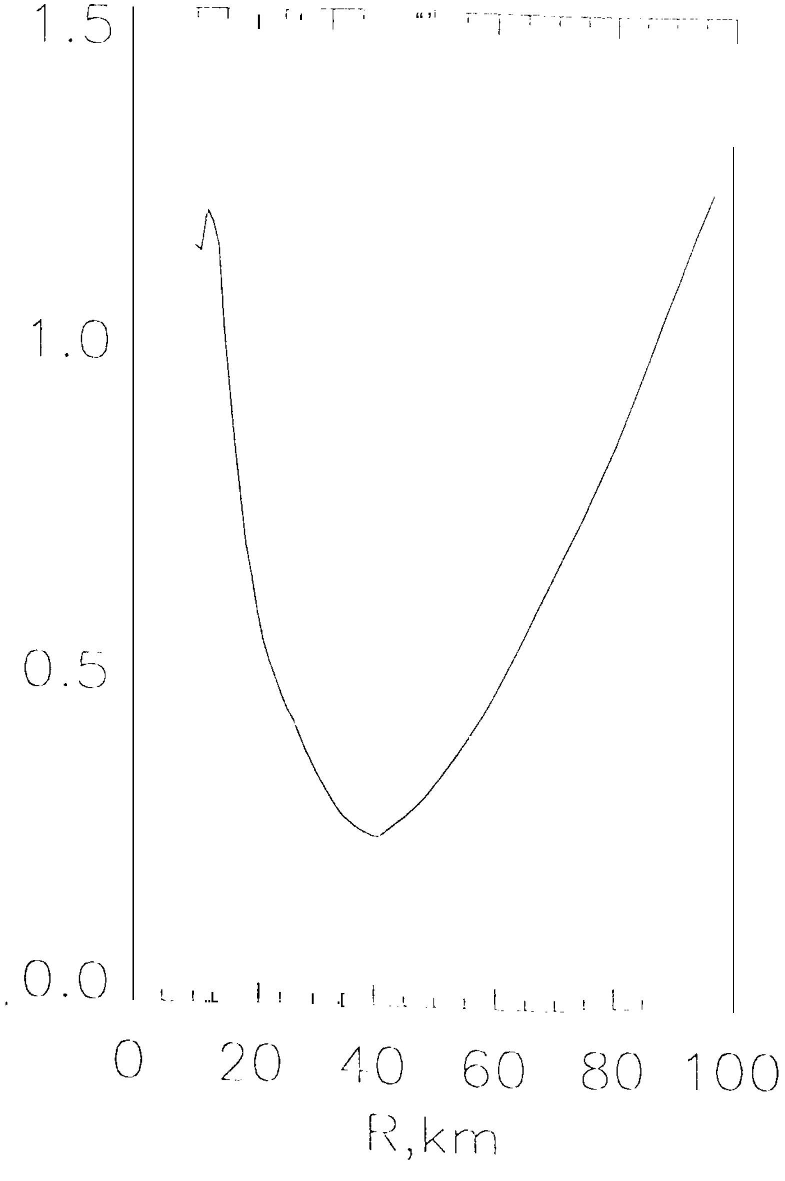

Fig. 14

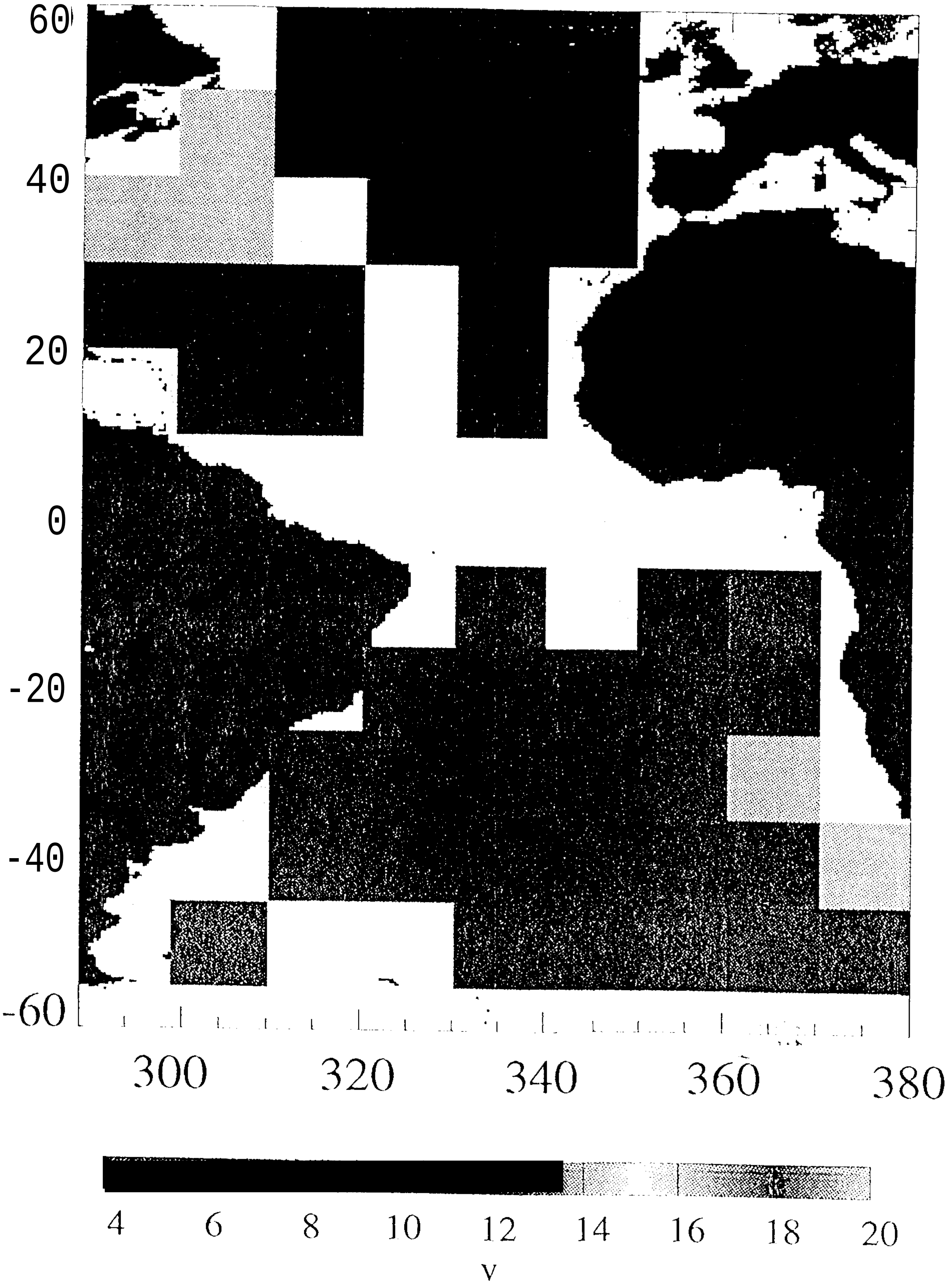
60
40
20
0
-20
-40
-60
300
320
340
360
380
4
6
8
10
12
14
16
18
20
V

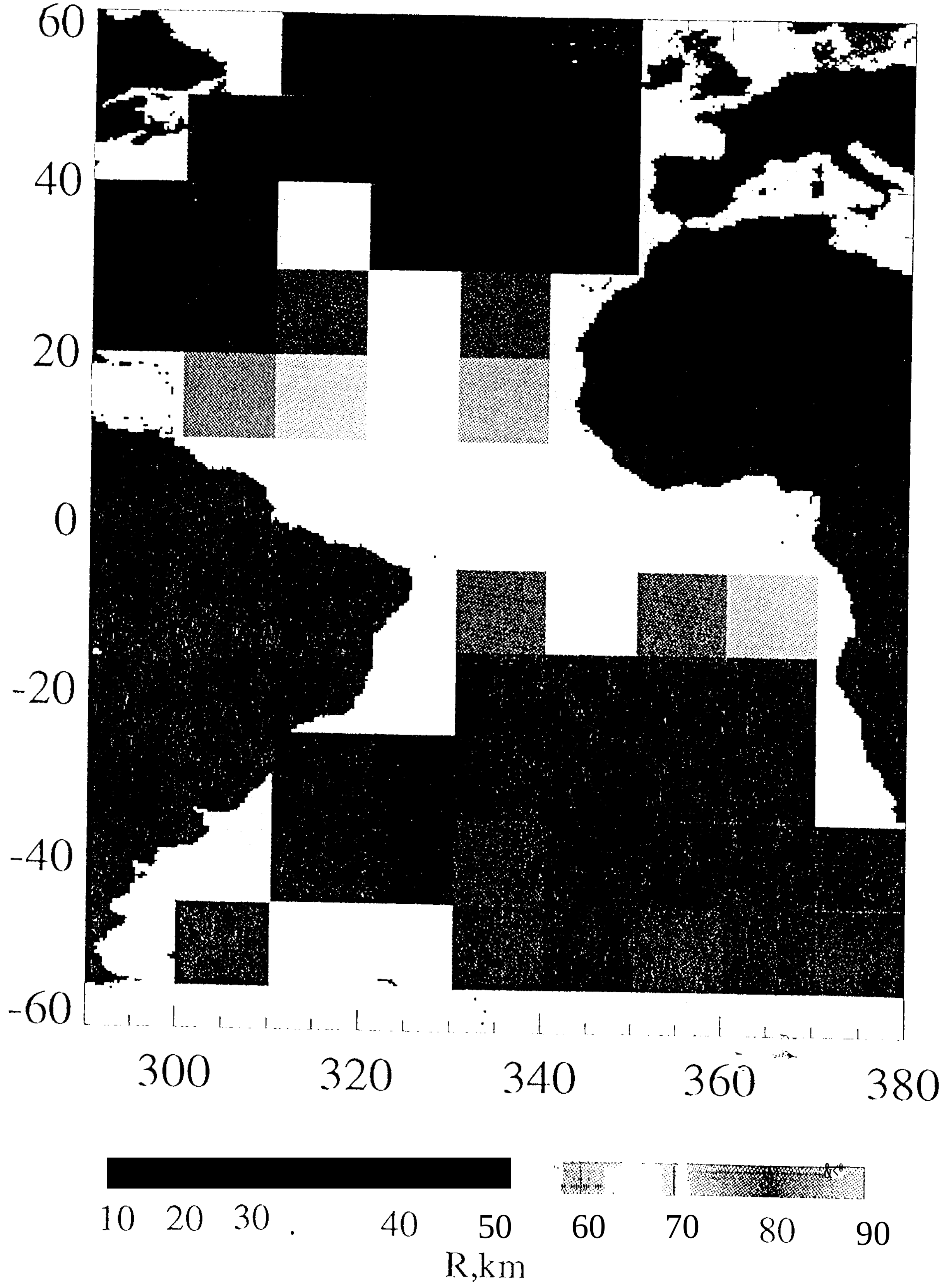
60
40
20
0
-20
-40
-60
300
320
340
360
380
10
20
30
40
50
60
70
80
90
R,km

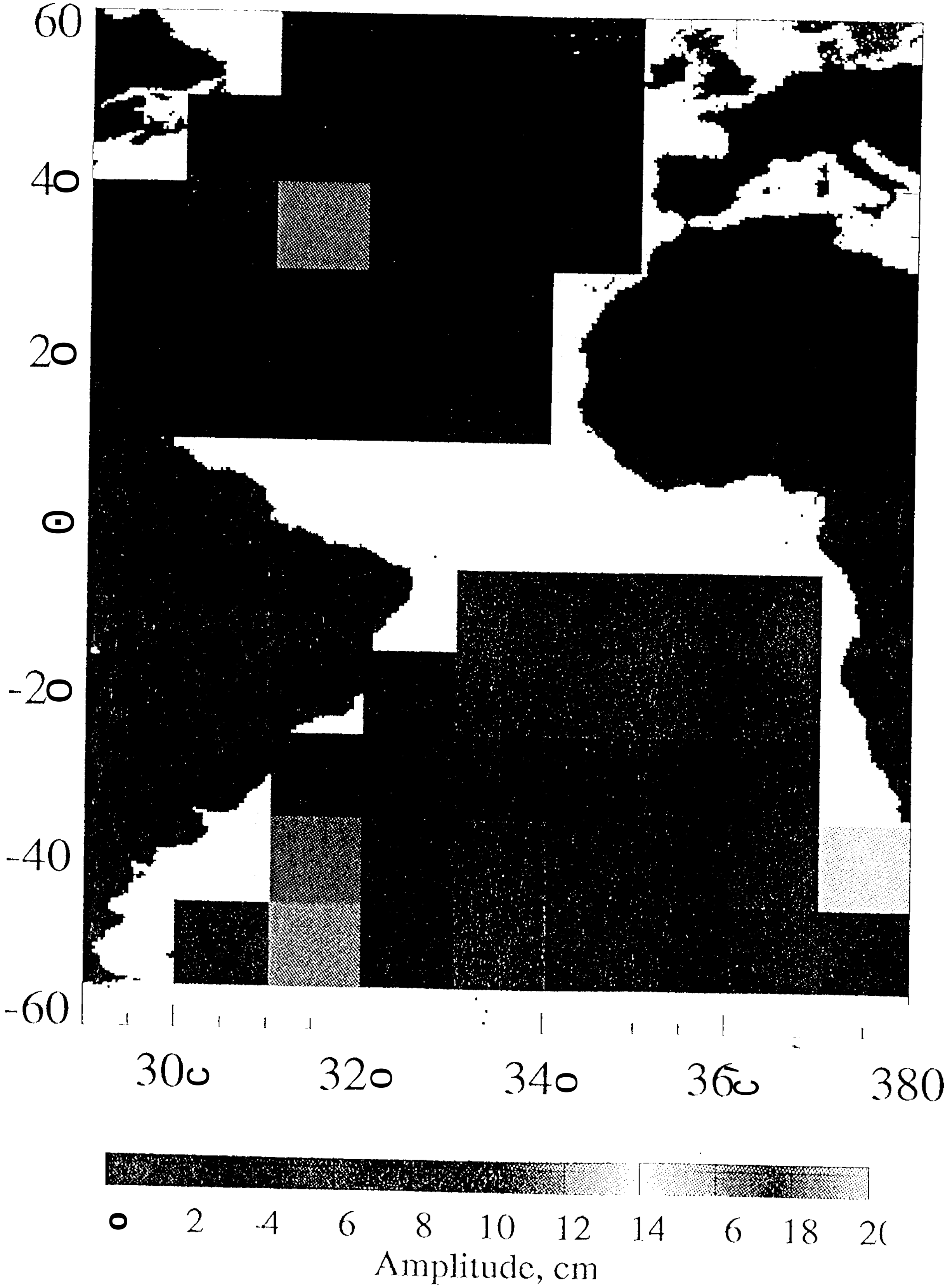
60
40
20
0
-20
-40
-60
300
320
340
360
380
0
2
4
6
8
10
12
14
16
18
20
Amplitude, cm